Remote Sensing of Environment 144 (2014) 11–27

Contents lists available at ScienceDirect

Remote Sensing of Environment

journal homepage: www.elsevier.com/locate/rse

Improved algorithms for accurate retrieval of UV/visible diffuse attenuation coefficients in optically complex, inshore waters

Fang Cao [a], Cédric G. Fichot [b], Stanford B. Hooker [c], William L. Miller [a,*]

[a] Department of Marine Sciences, University of Georgia, Athens, GA 30602, USA
[b] Marine Science Program, University of South Carolina, Columbia, SC 29208, USA
[c] Ocean Ecology Laboratory, NASA Goddard Space Flight Center, Greenbelt, MD 20771, USA

ARTICLE INFO

Article history:
Received 31 July 2013
Received in revised form 13 January 2014
Accepted 14 January 2014
Available online xxxx

Keywords:
Diffuse attenuation coefficient
Remote sensing reflectance
Ocean color
Algorithms
Ultraviolet radiation
Inshore waters
Global scale

ABSTRACT

Photochemical processes driven by high-energy ultraviolet radiation (UVR) in inshore, estuarine, and coastal waters play an important role in global biogeochemical cycles and biological systems. A key to modeling photochemical processes in these optically complex waters is an accurate description of the vertical distribution of UVR in the water column which can be obtained using the diffuse attenuation coefficients of downwelling irradiance ($K_d(\lambda)$). The Sea*UV*/Sea*UVc* algorithms (Fichot et al., 2008) can accurately retrieve K_d (λ = 320, 340, 380, 412, 443 and 490 nm) in oceanic and coastal waters using multispectral remote sensing reflectances ($R_{rs}(\lambda)$, SeaWiFS bands). However, Sea*UV*/Sea*UVc* algorithms are currently not optimized for use in optically complex, inshore waters, where they tend to severely underestimate $K_d(\lambda)$. Here, a new training data set of optical properties collected in optically complex, inshore waters was used to re-parameterize the original Sea*UV*/Sea*UVc* algorithms, resulting in improved $K_d(\lambda)$ retrievals for turbid, estuarine waters. Although the updated Sea*UV*/Sea*UVc* algorithms perform best in optically complex waters, the original Sea*UV*/Sea*UVc* models still perform well in most coastal and oceanic waters. Therefore, we propose a composite set of Sea*UV*/Sea*UVc* algorithms, optimized for $K_d(\lambda)$ retrieval in almost all marine systems, ranging from oceanic to inshore waters. The composite algorithm set can retrieve K_d from ocean color with good accuracy across this wide range of water types (e.g., within a mean relative error of 13% for $K_d(340)$). A validation step using three independent, *in situ* data sets indicates that the composite Sea*UV*/Sea*UVc* can generate accurate $K_d(\lambda)$ values at λ = 320–490 nm from ocean color on a global scale. Taking advantage of the inherent benefits of our statistical methods, we pooled the validation data with the training set, obtaining an optimized composite model for estimating $K_d(\lambda)$ in UV wavelengths for almost all marine waters. This "optimized composite" set of Sea*UV*/Sea*UVc* algorithms will provide the optical community with improved ability to quantify the role of solar UV radiation in photochemical and photobiological processes in the ocean.

1. Introduction

Solar ultraviolet radiation (UVR; 280–400 nm) is a critical factor in regulating the biogeochemical cycles in the ocean (Whitehead, de Mora, & Demers, 2000). High-energy UVR is the driving factor for the photooxidation of colored dissolved organic matter (CDOM), the dominant UVR-absorbing component within the larger pool of dissolved organic carbon (DOC), especially in coastal areas and estuaries (Mopper & Kieber, 2000). The photochemical degradation and mineralization of CDOM can therefore have an important effect on biogeochemical carbon cycling in the ocean. UVR also impacts bacterial and photosynthetic activity through DNA damage and repair processes in natural waters (Sinha & Häder, 2002; Tedetti & Sempéré, 2006).

Quantitative assessment of *in situ* photochemical and photobiological processes can benefit from knowledge of the vertical distribution of UV and visible radiation in natural waters (Fichot & Miller, 2010). The diffuse attenuation coefficient, $K_d(\lambda)$, is defined as the fractional rate of decay of downwelling spectral irradiance with depth and can be used to calculate vertical profiles of irradiance in the water column from measurements of surface irradiance (Kirk, 1994). The diffuse attenuation coefficient depends not only on the optically active water constituents, but also on the distribution of the ambient light field (solar zenith angle, surface and sky conditions, etc.) (Lee, Du, Arnone, Liew, & Penta, 2005). K_d spans several orders of magnitude between the clearest oceanic waters (e.g., surface subtropical gyres) and the darkest inshore waters (e.g., dark oligotrophic lakes) (Booth & Morrow, 1997; Kjeldstad et al., 2003). Satellite imagery could therefore facilitate the quantification of K_d over large temporal and spatial scales.

The determination of K_d is amenable to the remote sensing of ocean color. Austin and Petzold (1981) first proposed an empirical relationship between K_d and a blue-green ratio of water-leaving radiance ($L_w(443)/L_w(555)$) in order to facilitate the retrieval of $K_d(490)$ from ocean-color remote sensing. Previous efforts of K_d retrieval for Case 1 and Case 2 waters generally included only visible bands, and were based on either

* Corresponding author. Tel.: +1 706 542 4299.
E-mail address: bmiller@uga.edu (W.L. Miller).

0034-4257/$ – see front matter © 2014 Elsevier Inc. All rights reserved.
http://dx.doi.org/10.1016/j.rse.2014.01.003

Table 1
Sampling information for the data used in this study ($N = 438$).

Location	Date	No. of samples
UCSB/Dalhousie dataset	1996–2002	333
South Atlantic Bight (SAB)	May 2006	15
SOLAS Autumn Cruise (SABINA)	2003	4
Mid-Atlantic Bight (MAB)/Gulf of Maine	July 2002	12
Georgia coast	2006–2011	74

empirical or semi-analytical methods (Jamet, Loisel, & Dessailly, 2012; Johannessen, Miller, & Cullen, 2003; Kuhn, Browman, McArthur, & St-Pierre, 1999; Mueller, 2000). However, few studies have focused on the retrieval of K_d in the UV domain, especially in turbid estuaries. Fichot, Sathyendranath, & Miller (2008) recently developed the Sea*UV* and Sea*UVc* algorithms for the retrieval of $K_d(\lambda)$ ($\lambda = 320$–490 nm) from multispectral remote-sensing reflectances ($\lambda = 412$–670 nm) in the ocean. These algorithms were developed and validated for coastal and open ocean waters. However, these algorithms can severely underestimate K_d retrievals in the UV when applied to inshore waters (as shown later in Section 3.1). This clearly calls for a refined approach and tuning of the original model for improved accuracy of $K_d(\lambda)$ retrievals in optically complex inshore waters.

In this study, *in situ* measurements of optical properties collected in turbid, CDOM-rich coastal and inshore areas are used to enhance the applicability of Sea*UV* and Sea*UVc* algorithms in optically complex waters. This new data set is used along with the original training data set of Fichot et al. (2008) to develop and validate a "composite Sea*UV* and Sea*UVc*" algorithm set optimized for water types ranging from blue oceanic to highly productive, turbid inshore waters (see Table 1). This new algorithm set will enhance our capability to monitor the *in situ* attenuation of solar radiation (UV–visible) and quantify photochemical and photobiological processes in most natural waters.

2. Data and approach

2.1. Background of current SeaUV algorithms

The Sea*UV*/Sea*UVc* algorithms can be used to retrieve $K_d(\lambda)$ at $\lambda = 320$, 340, 380, 412, 443 and 490 nm from spectral remote-sensing reflectance ($R_{rs}(\lambda)$) in the visible range. The basic approach uses a principal component analysis (PCA) to collapse $R_{rs}(\lambda)$ spectra ($\lambda = 412$, 443, 490, 510, 555 and 670 nm) into four principal components (PCs). Multilinear regressions were then parameterized between measured *in situ* $K_d(\lambda)$ and the four PCs, resulting in a model named Sea*UV*. In Sea*UVc*, a cluster analysis was applied to the first two PC scores in order to divide the ocean color data set into distinct ocean color domains based on the $R_{rs}(\lambda)$ spectral characteristics. This classification allowed the derivation of ocean color domain-specific multi-linear parameters. The use of PCs in Sea*UV* and Sea*UVc* resulted in a more complete utilization of the multispectral information contained in $R_{rs}(\lambda)$ spectra, and provided more accurate $K_d(\lambda)$ retrievals compared to traditional band-ratio methods that only use R_{rs} at two wavelengths (Fichot et al., 2008). In the rest of this manuscript, the Fichot et al. (2008) algorithms are referred to as the "original" Sea*UV*/Sea*UVc* model.

2.2. Study area and data collection

Sampling was conducted in three distinct estuarine systems along the Southeastern coast of the U.S. (Altamaha, Doboy and Sapelo sounds in Georgia) (Fig. 1). A total set of 74 *in situ*, simultaneous measurements of $R_{rs}(\lambda)$ and $K_d(\lambda)$ were collected in June 2006, February 2007, August 2009, July 2010, March 2011, and June 2011. The three sampled estuarine systems had distinct hydrological settings. The Altamaha Sound is a river-dominated site and receives freshwater inputs and large amounts of suspended particles from the Altamaha River. It is generally

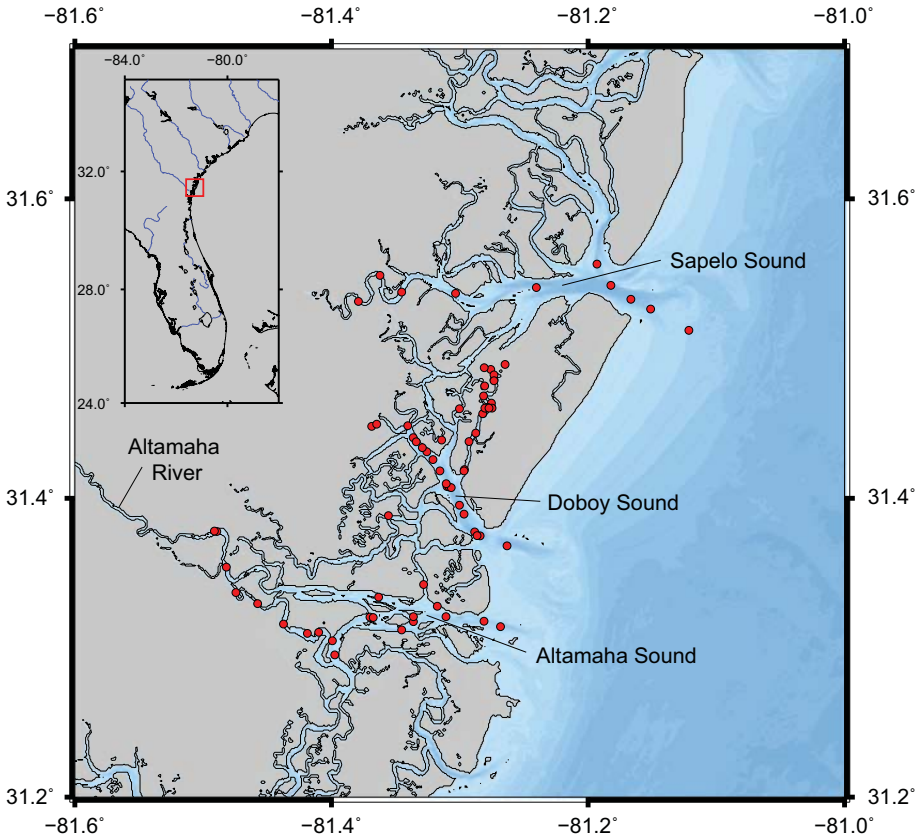

Fig. 1. Map of optically complex inshore waters sampled along coastal Georgia during 2006–2011. The coastline data was downloaded from the NOAA National Geophysical Data Center (http://www.ngdc.noaa.gov/mgg/shorelines/shorelines.html).

characterized by high loadings (~30 mg/l) of total suspend solids (TSS) (Witte et al., 1982). The optical properties of the Altamaha Sound are further complicated by the organic matter accumulation promoted by freshwater input from the Altamaha River (Craft, 2007). Doboy Sound is located to the north of Altamaha Sound and is a tidal marsh-dominated site. It can receive significant riverine input from the Altamaha River during high flow seasons (usually February to April). Sapelo Sound is the northernmost site sampled and is a coastal, marine-dominated site, comparatively more saline and experiencing less hydrological variation than its neighboring estuaries to the south (Richardson & LeDrew, 2006). The study area spanning the three estuarine systems is characterized as a CDOM-rich ($a_{CDOM}(300)$ up to 13 m^{-1}) and highly dynamic system with periodic heavy loads of suspended particles.

Two optical instruments were deployed at each sampling station and all measurements were taken within 2 h of solar noon (solar zenith angle (SZA) varied in the range of 15° ~ 35°) in order to preserve the quasi-inherent property of the diffuse attenuation coefficient (Gordon, 1989). A Satlantic® multispectral profiling radiometer (MicroPRO, with wavebands centered at λ = 305, 325, 340, 380, 412, 443, 490, 555 nm) was deployed three or more times at each station to measure profiles of spectral downwelling irradiance ($E_d(\lambda, z)$, μW cm^{-2} nm^{-1}). The MicroPRO was either lowered slowly by hand on the sunny side of a small vessel or floated away and used in free-fall mode depending on data density and orientation requirements. Data with instrument tilt greater than 5° was removed before algorithm development. The optical depth, $\zeta(\lambda, z)$, was calculated as in Eq. (1):

$$\zeta(\lambda, z) = -\ln(E_d(\lambda, z)/E_d(\lambda, 0^-)) \quad (1)$$

where $E_d(\lambda,0^-) \approx E_d(\lambda,0^+)/1.04$, (Austin, 1974; Kirk, 1994).

The diffuse attenuation coefficient, $K_d(\lambda)$, was calculated as in Eq. (2):

$$K_d(\lambda) = \zeta(\lambda, z)/z \quad (2)$$

where z is the water depth at which the detection limit of the instrument is reached. Typical z values were <0.5 m for K_d (340) and no optical stratification was noted over this depth.

Paired Satlantic® multispectral OCR507 radiometers mounted on a buoy were used to measure above-surface remote-sensing reflectance ($R_{rs}(\lambda,0^+)$, sr^{-1}) at λ = 305, 325, 340, 380, 412, 443, 490, 510, 555, 670, and 683 nm. The OCR system was deployed on the sunny side of the boat, and at the same time as the MicroPRO in order to obtain simultaneous measurements of $K_d(\lambda)$ and $Rrs(\lambda)$. The OCR system measured simultaneously above-surface downwelling irradiance ($E_d(\lambda,0^+)$, μW cm^{-2} nm^{-1}) and just-below-surface (~2–3 cm) upwelling radiance ($L_u(\lambda, 0^-)$, μW cm^{-2} nm^{-1} sr^{-1}). Water-leaving radiance, $L_w(\lambda)$, was then derived from $L_u(\lambda, 0^-)$ using the approximation $L_W(\lambda) \approx 0.54 * L_u(\lambda,0^-)$ of Austin (1974). The $R_{rs}(\lambda,0^+)$ was then calculated as the ratio of $L_w(\lambda)$ over $E_d(\lambda,0^+)$ for the following wavelengths: λ = 412, 443, 490, 510, 555 and 670 nm. Due to high levels of CDOM and turbidity, bottom effects on the determination on R_{rs} can be neglected and the study area is considered to be optically deep. The MicroPRO and OCR were re-calibrated annually by Satlantic, Inc. Uncertainties (such as sun elevation, surface extrapolations, etc.) associated with R_{rs} and K_d measurements are detailed in Fichot et al. (2008).

2.3. Optimization of original SeaUV algorithms for optically complex, inshore waters

In a first attempt to optimize the algorithms, the inshore-water data set collected in this study ($N = 74$) was pooled into the original training data set of Fichot et al. (2008), and the models were re-parameterized using the exact same approach as the one used in Fichot et al. (2008). However, simple re-parameterization using this updated data set ($N = 438$) did not achieve better overall performance (see Supplementary material). To better estimate K_d in inshore waters and maintain the good performance of original algorithms of K_d retrieval in open ocean waters as well, the original approach used by Fichot et al. (2008) was therefore modified to optimize the performance of the algorithms from open ocean waters to optically complex inshore waters.

2.3.1. Determination of the cutoff point for inshore waters

The new approach to improve the performance of the original Sea*UV*/Sea*UVc* algorithms for inshore waters was developed by re-parameterizing the multi-linear equations with a re-defined, inshore water training data set split from the complete data set. In the rest of this manuscript, the models developed with this new approach are referred to as "inshore-water optimized" Sea*UV*/Sea*UVc*. A cutoff value based on $K_d(490)$ was defined to distinguish inshore waters for which Sea*UV*/Sea*UVc* should be optimized. $K_d(490)$ was chosen to distinguish inshore waters from other water types for two reasons. First, $K_d(490)$ gave the least accurate retrieval when the original Sea*UV*/Sea*UVc* was applied to our new inshore water data (as shown later in Section 3.2).

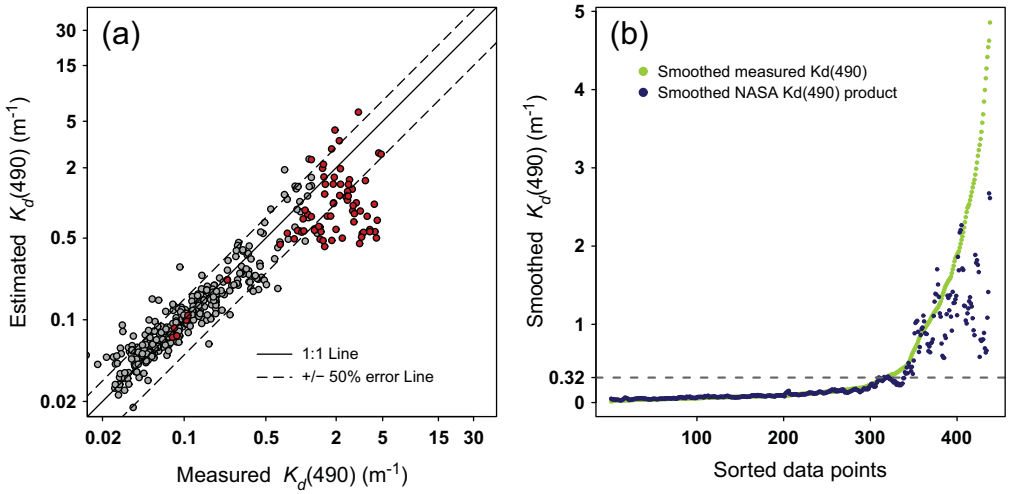

Fig. 2. Determination of the cutoff point for the inshore water optimized Sea*UV*/Sea*UVc* algorithms. (a) Performance of the latest NASA $K_d(490)$ product on the complete training data set. Filled red circles mark K_d collected along coastal Georgia and gray circles represent K_d published by Fichot et al. (2008). (b) Smoothed results from the five-point moving-average function applied to measured *in situ* K_d data (filled green circles) and modeled K_d derived from the latest NASA $K_d(490)$ product (filled blue circles), respectively. The x-axis represents the data points sorted in ascending order ($N = 438$) based on measured *in situ* $K_d(490)$. The y-axis represents corresponding smoothed $K_d(490)$ values. (For interpretation of the references to color in this figure legend, the reader is referred to the web version of this article.)

Second, $K_d(490)$ is a standard NASA product from SeaWiFS data that allows a determination of water type with AOP's external to the Sea*UV*/Sea*UVc* implementation. This eliminates potential internal bias when applying our new approach to remotely sensed ocean color.

To determine the cutoff point, we first sorted the measured *in situ* $K_d(490)$ in ascending order and then applied a five-point moving-average smoothing function to both the measured *in situ* $K_d(490)$ and estimated $K_d(490)$ values retrieved from the latest NASA $K_d(490)$ product (Werdell, 2009). Fig. 2(a) displays the performance of the $K_d(490)$ product on our complete data set. The cutoff point was chosen to be at the point where the measured $K_d(490)$ began to diverge from the estimated values in the $K_d(490)$ product. By examining the smoothed curve in Fig. 2(b), the cutoff point was determined to be 0.32 m^{-1} for $K_d(490)$. Any measured $K_d(490)$ values in the combined data set which was greater than 0.32 m^{-1} was considered as optically complex inshore water, giving a total of 119 points to be included in the inshore water training data used to derive the new parameters for the inshore-water optimized *SeaUV* algorithms.

2.3.2. Optimization of SeaUV/SeaUVc algorithms for inshore waters

The inshore water training data set ($N = 119$) was first log-transformed and then re-standardized following Eq. (2) in Fichot et al. (2008). To optimize the Sea*UV* algorithms for inshore waters, the re-standardized $R_{rs}(\lambda)$ data of the inshore water training data set ($N = 119$) were combined into four principal components, and regression coefficients were generated by fitting a multi-linear relationship between the four PC scores and the measured K_d values. A fuzzy c-means cluster analysis (FCM) was then applied to the two-dimensional (2-D) data set spanned by the first two PC scores generated in the inshore-water optimized Sea*UV*. We used the c-means function in the R software package (http://www.r-project.org/) to carry out the cluster analysis. The algorithms are based on minimizing the objective function defined as follows in Eq. (3):

$$J_m = \sum_{i=1}^{N}\sum_{j=1}^{C}\mu_{ij}^{m}\left\|x_i - c_j\right\|^2 \tag{3}$$

where m is the weighting component; x_i is the ith observation in the 2D dataset spanned by the first two PCs; c_j defines the cluster centers in the 2D dataset; μ_{ij} is the degree of membership of x_i to the cluster j, and $\|x_i - c_j\|$ is the Euclidean norm which represents the similarity between the measured data and the cluster centers (Moore, Campbell, & Dowell, 2009). Evaluated by multiple fuzzy cluster indexes (e.g. partition coefficient, partition entropy, etc.), four representative dark water ocean color domains (DWDs) were defined and the cluster centers were determined when the optimization criteria were satisfied (Moore, Campbell, & Feng, 2001). This use of FCM (also known as the soft *K*-means clustering method) is the only difference between the current approach and the original Fichot et al. (2008) method, which applied a hard *K*-means clustering method. Through the membership assignment of every data point to different clusters, FCM provides more robust estimation of cluster centers than the hard *K*-means method, where cluster centers must be optimized through many trails. Another advantage of applying FCM over the conventional hard *K*-means method is that the number of clusters can be optimized and validated through multiple validity indexes, a more objective and convincing method than the pre-specified cluster numbers from hard *K*-means method. Fig. 3 shows the $R_{rs}(\lambda)$ spectra for the four dark water domains. The numbers of samples assigned to each of the four DWDs are 20, 31, 31 and 37, respectively.

2.4. Development of composite SeaUV/SeaUVc algorithms

The original Sea*UV* algorithms still performed best in open ocean and coastal waters, where $K_d(490) < 0.32\ m^{-1}$. In order to optimize the overall performance of the algorithms in the full range of natural water types, we assembled and tested a composite version of the algorithms. This composite algorithm uses the original Sea*UV*/Sea*UVc* for open ocean and coastal waters (where $K_d(490) < 0.32\ m^{-1}$), and the inshore-water optimized Sea*UV*/Sea*UVc* for optically complex waters (where $K_d(490) \geq 0.32\ m^{-1}$).

2.5. Accuracy assessment

The mean relative error (MRE(λ)) was calculated in order to evaluate the accuracy of $K_d(\lambda)$ retrievals and the overall performance of the original, inshore-water optimized, and composite Sea*UV*/Sea*UVc* algorithms. The MRE(λ) is defined in Eqs. (4a) and (4b) as follows:

$$MRE(|\overline{\varepsilon}|,\lambda) = \frac{1}{N}\sum_{i=1}^{N}|\varepsilon_i|(\lambda) \tag{4a}$$

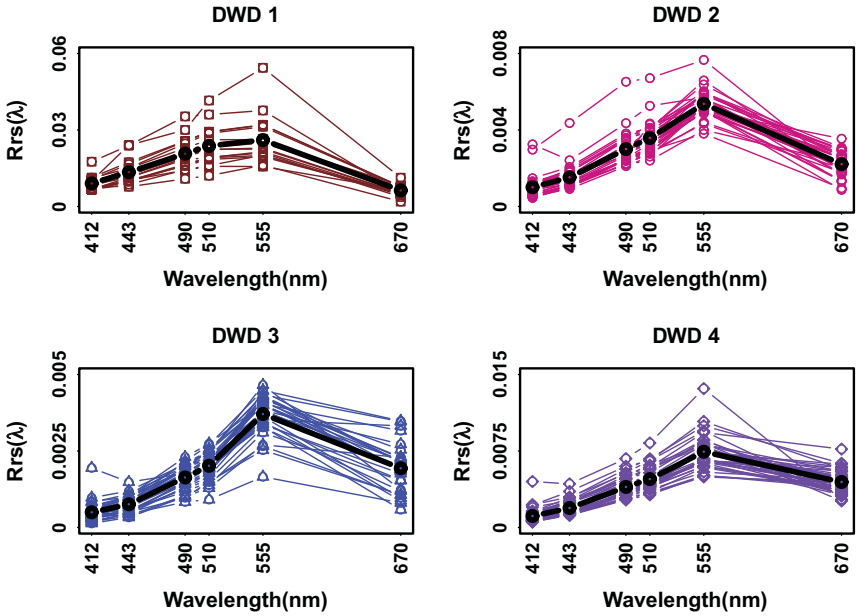

Fig. 3. Remote sensing reflectance spectra (R_{rs}) in the four statistically determined dark water domains (DWDs). The spectra in black represent the mean R_{rs} values for each dark water domain.

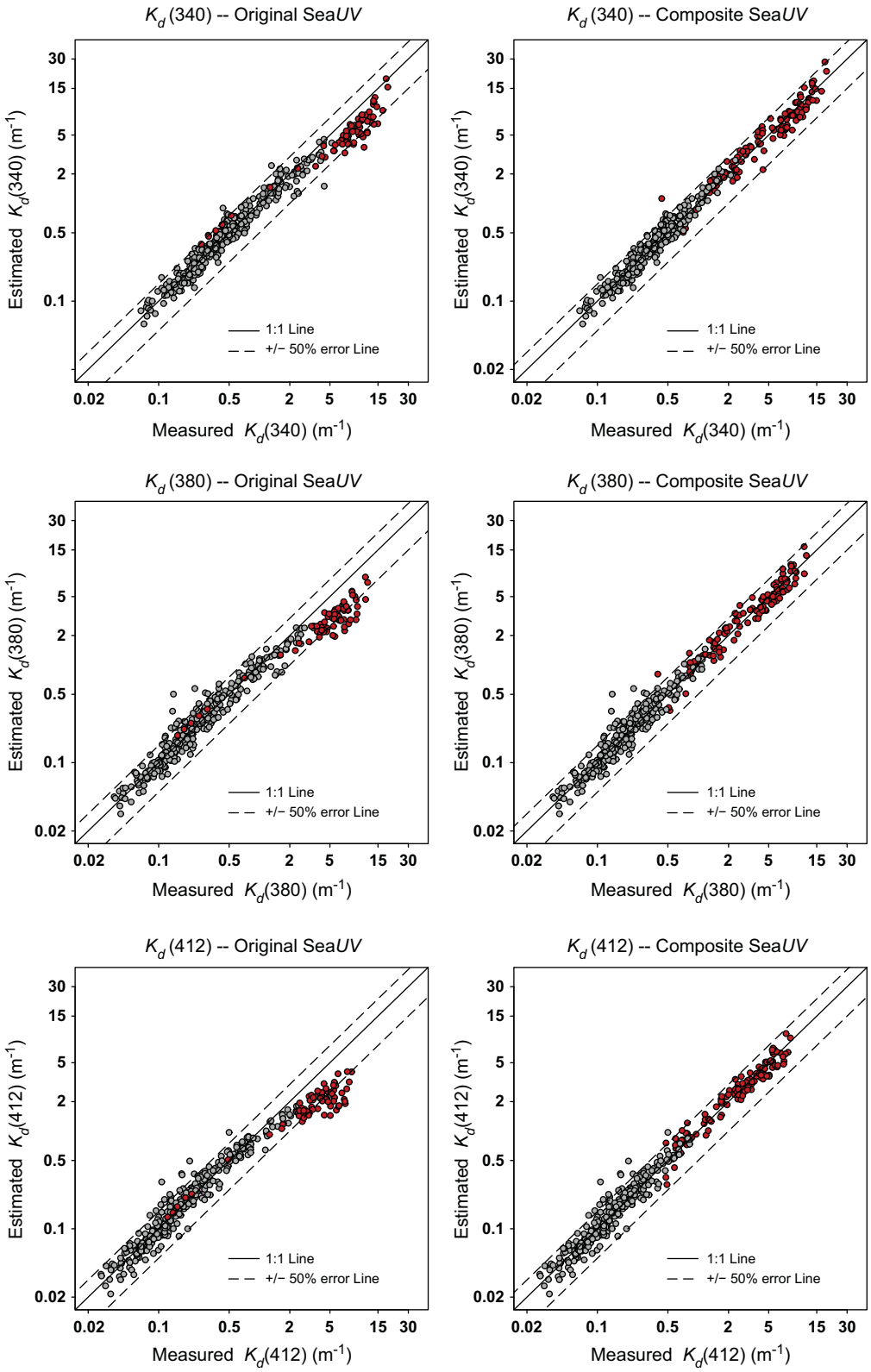

Fig. 4. Comparisons of measured *in situ* K_d with calculated K_d derived from original Sea*UV* and composite Sea*UV* algorithms at $\lambda = 340$, 380 and 412 nm. In the panels at the left, filled red circles ($N = 74$) mark K_d collected along the Georgia coast and gray circles ($N = 364$) denote K_d published in Fichot et al. (2008). In the panels on the right, filled red circles ($N = 119$) represent the inshore water training data set ($N = 119$) split from the complete training data set and gray circles represent all data collected not in the inshore water training data set. (For interpretation of the references to color in this figure legend, the reader is referred to the web version of this article.)

where

$$\varepsilon_i = 100 * \frac{K_d(\lambda)^{estimated} - K_d(\lambda)^{measured}}{K_d(\lambda)^{measured}} \quad (4b)$$

and where i is the index number, and N is the number of observations. Note that $K_d(\lambda)$ values measured at $\lambda = 325$ and $\lambda = 340$ nm were linearly extrapolated to calculate the $K_d(\lambda)$ value at $\lambda = 320$ nm to allow direct accuracy comparison to the original Sea*UV*/Sea*UVc* results.

3. Results and discussion

3.1. Evaluation of original SeaUV algorithms for inshore waters

The original Sea*UV* algorithms were first implemented using the complete data set of $R_{rs}(\lambda)$ spectra that includes our new inshore-water stations. As shown in Figs. 4, 5 and 6, the $K_d(\lambda)$ values derived in inshore waters using the original Sea*UV* algorithms are underestimated relative to the measured *in situ* $K_d(\lambda)$. The bias increases as values for $K_d(\lambda)$ increase and the underestimation is more distinct when the original Sea*UVc* was applied to the inshore water data set alone. For example, in Fig. 6, the original Sea*UVc* generates higher

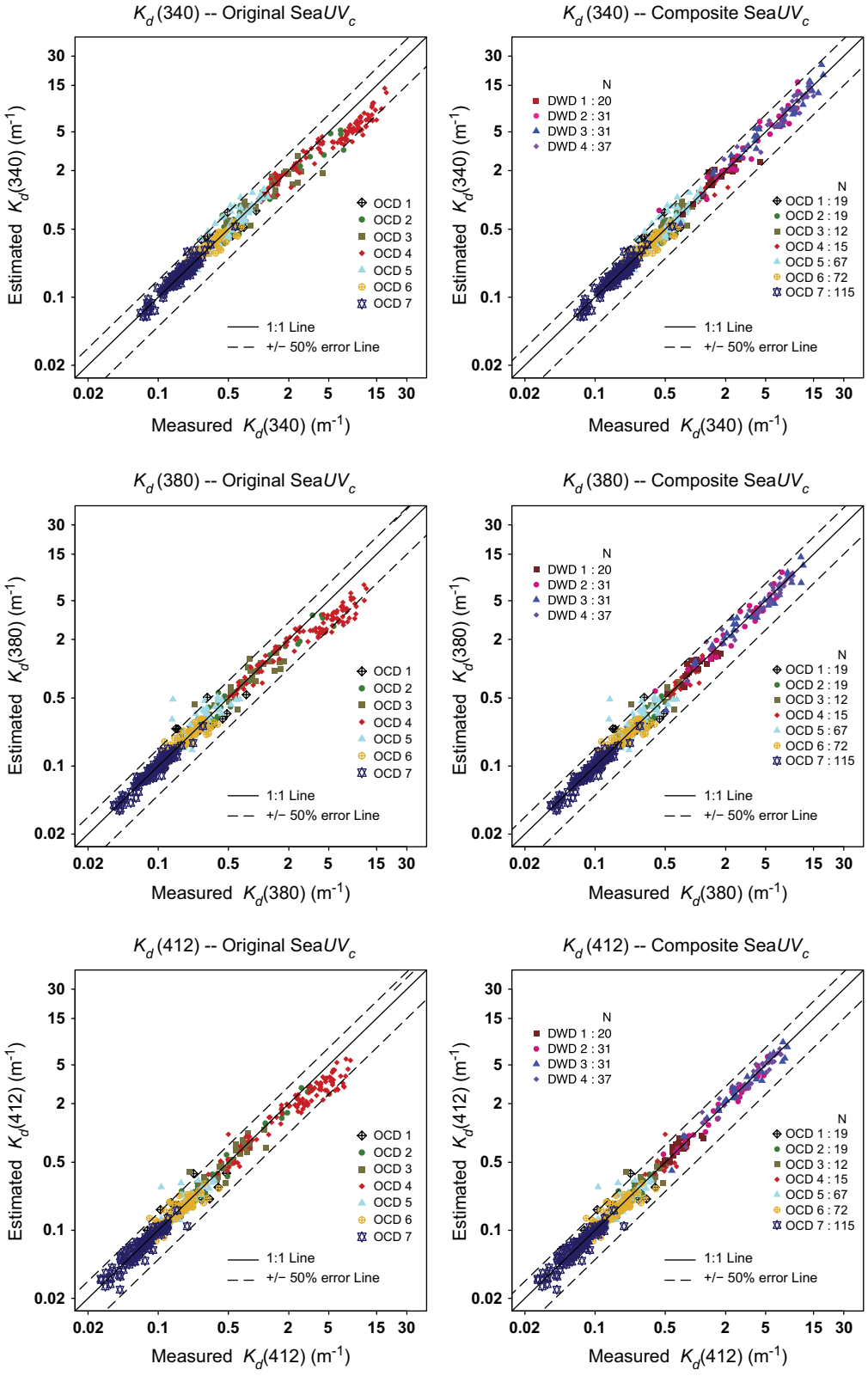

Fig. 5. Comparisons of measured *in situ* K_d with calculated K_d derived from original Sea*UVc* and composite Sea*UVc* algorithms at $\lambda = 340$, 380 and 412 nm.

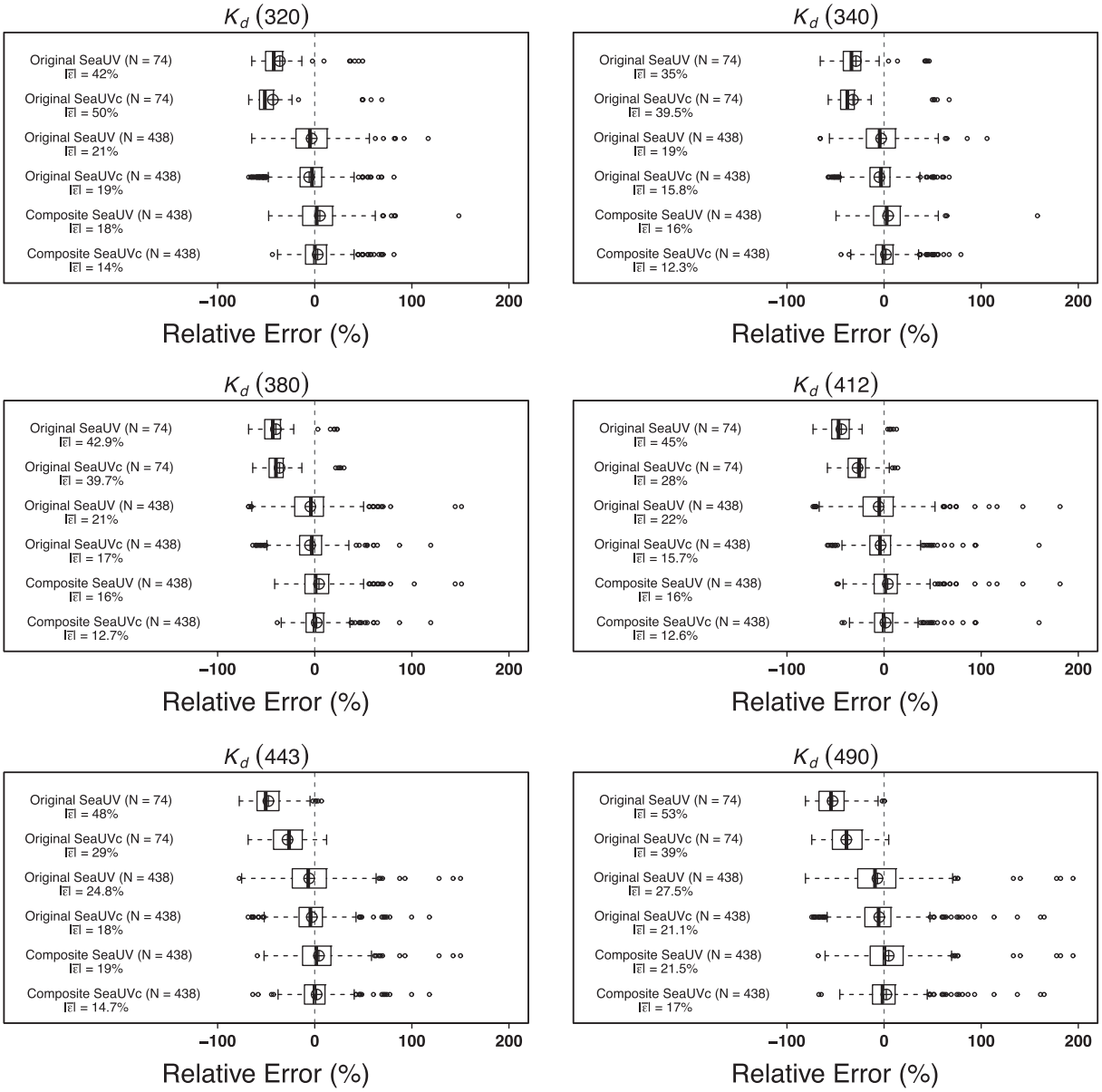

Fig. 6. Box and whisker plots of relative error distribution of K_d derived from the original and composite Sea*UV*/Sea*UVc* algorithms at λ = 320, 340, 380, 412, 443 and 490 nm for the inshore data set collected in this study ($N = 74$) and complete training data set ($N = 438$). The circle plus symbol in each boxplot represents the mean relative error (MRE, $|\bar{\varepsilon}|$).

biases and performs more poorly for $K_d(320)$ than Sea*UV*. The accuracy of $K_d(490)$ estimated in inshore waters using the original Sea*UVc* shows slightly better performance than Sea*UV*, but remains low. The severe underestimation of estimated K_d values in inshore waters reflects the fact that the original Sea*UV*/Sea*UVc* algorithms were parameterized for coastal and open ocean water. In optically complex inshore waters, K_d values are higher (e.g. at Altamaha Sound, with $K_d(340) \sim 18.7\ m^{-1}$) and extend out of the range for which the model was originally developed, most likely contributing to its inability to accurately predict K_d in the new inshore water data set.

3.2. Performance assessment of inshore-water optimized SeaUV/SeaUVc algorithms

Instead of simply re-parameterizing the original model with an expanded data set that included an extended K_d range, our cutoff point ($K_d(490) = 0.32\ m^{-1}$) was applied for the inshore-water optimized algorithms to distinguish optically complex inshore waters from the other water types. Data with $K_d(490)$ values above the cutoff point were classified as optically complex ($N = 119$) and were used as a separate training data set for parameterizing the inshore-water optimized algorithms. MRE values derived from the inshore-water optimized algorithms are significantly reduced compared to those derived using the original Sea*UV* algorithms (e.g. for $K_d(380)$, MRE = 17.6% from inshore-water optimized algorithms, compared to MRE = 42.9% from original Sea*UV*, error distribution and fitting parameters as shown in the Supplementary material).

While K_d in inshore waters is generally retrieved with good accuracy at most wavelengths after optimization, retrieval of $K_d(320)$ using the inshore-water optimized Sea*UV* algorithms yields higher errors compared to the K_d estimates at longer wavelengths (MRE for $K_d(320)$ = 21.4%, compared to MRE = 15% for $K_d(412)$). This higher error for $K_d(320)$ could be related to the difficulty of measuring K_d at UV wavelengths in highly colored waters. Since most of the apparent optical properties (AOPs) in the optically complex water training data set used to parameterize the inshore-water optimized Sea*UV* algorithms were collected in coastal Georgia waters (high CDOM and particulate load), measurements of downward UV irradiance generally rapidly

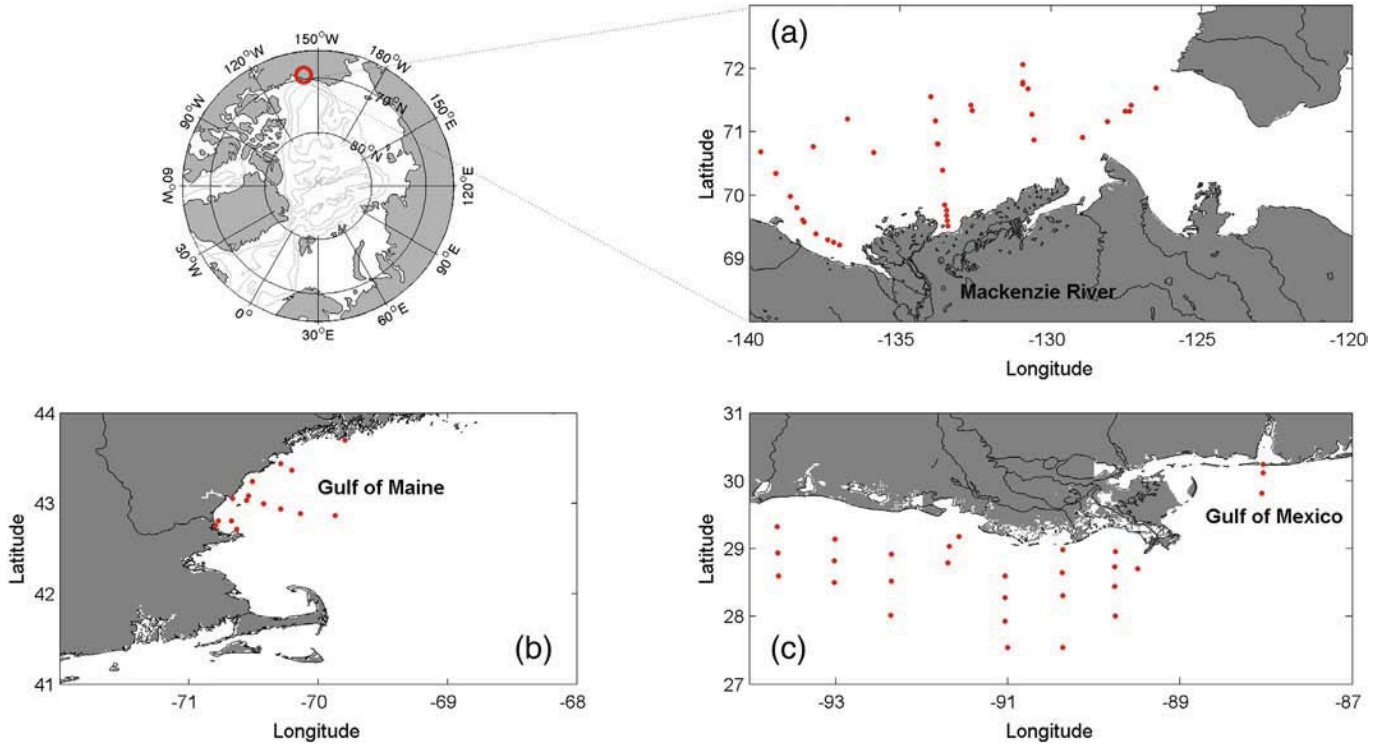

Fig. 7. Locations of stations for *in situ* paired AOP data used as the validation data set ($N = 125$): (a) Mackenzie River outflow during the MALINA cruise, (b) Gulf of Maine, and (c) Northern Gulf of Mexico (collected during five GulfCarbon cruises).

falls below the detection limits of the instrument during profiling. The measured *in situ* $K_d(320)$ data likely contained more inaccuracy than longer wavelengths when parameterizing of the algorithms. In addition, the strong attenuation of UV radiation in dark water requires K_d measurements to be made very close to the water surface where wave-induced fluctuations may contribute larger variations to the spectral irradiance measurement (Laurion, Vincent, & Lean, 1997; Markager & Vincent, 2000; Tedetti et al., 2007). These challenges of K_d measurements at shorter UV wavelengths in optically complex waters could explain the increasing uncertainty of K_d values observed at shorter wavelengths.

3.3. Evaluation of composite SeaUV algorithms

The composite Sea*UV* algorithms improved the accuracy of retrieved K_d in inshore waters. Figs. 4, 5 and 6 display the K_d retrievals with their relative error distributions that result from use of the composite Sea*UV*/Sea*UVc* algorithms applied to the entire training data set ($N = 438$). The good agreement between measured and retrieved K_d values demonstrates the improved overall performance of the composite Sea*UV*/Sea*UVc* algorithms (e.g. for $K_d(380)$, MRE = 16% from composite Sea*UV*, compared with MRE = 21% from original Sea*UV*).

The approach used in the composite Sea*UV* algorithms is similar to the merged $K_d(490)$ product for Chesapeake Bay developed by Wang, Son, and Harding (2009), which combines two separate empirical algorithms for $K_d(490)$ retrieval of open ocean and turbid coastal waters to derive $K_d(490)$ from satellite measurements. Good results for K_d retrieval using our composite algorithms result partly from accurate determination of the cutoff point ($K_d(490) = 0.32\ m^{-1}$) used to separate the fitting parameters for the composite algorithms. In the merged $K_d(490)$ product generated by Wang et al. (2009), using a completely separate data set, the same cutoff point of $K_d(490) = 0.3\ m^{-1}$ was proposed to distinguish the open ocean water with turbid coastal water. The combination of the two individual parts in the composite algorithms, with each part applicable to different water types, maximizes our ability to accurately predict K_d through the UV wavelength range in both open ocean and turbid inshore waters.

3.4. Sensitivity analysis of the cutoff point

By using the latest NASA $K_d(490)$ product to determine the switch point between different parts in the composite Sea*UV*/Sea*UVc* algorithms, it is possible that the error (~25%) in determining $K_d(490)$ for our training dataset, particularly for open ocean water ($K_d(490) < 0.32\ m^{-1}$), could translate to increased error in our ability to choose the $K_d(490)$ value that will prompt a switch between algorithms. We investigated the sensitivity of our retrieval accuracy using the composite Sea*UV* algorithms, by varying the cutoff point over the ranging between 0.16 and 0.36 m^{-1} for $K_d(490)$, corresponding to the ±25% error limits of the cutoff point derived from the $K_d(490)$ product. The estimated K_d (λ, λ = 320, 340, 380, 412, 443 and 490 nm) for our training dataset obtained by varying the cutoff point ±25% showed no statistically significant differences from the calculated $K_d(\lambda)$ values obtained with the cutoff point value set at $K_d(490) = 0.32\ m^{-1}$ (*t*-tests, with *p*-value > 0. 05 for $K_d(\lambda)$ at each wavelength, $N = 438$). Hence, the use of our $K_d(490) = 0.32\ m^{-1}$ switch point between clear and dark algorithms is not sensitive to the error associated implicitly with retrieval of the $K_d(490)$ product.

3.5. Validation of the composite SeaUV algorithms

Three independent sets of *in situ* AOPs were used to test the applicability of the composite Sea*UV*/Sea*UVc* algorithms. Paired measurements of $R_{rs}(\lambda)$ and $K_d(\lambda)$ were collected seasonally in the northern Gulf of Mexico (GulfCarbon cruises, 2009–2010), around the Mackenzie River outflow (MALINA cruise, August 2009), and the Gulf of Maine in 2008 (Fig. 7). The measured *in situ* $K_d(\lambda)$ in the validation data set cover different water types and span almost the same wide range as the

data used to parameterize the composite algorithms (e.g. for $K_d(380)$, the measured values span from 0.04 m^{-1} to 11.22 m^{-1}).

The validation procedure for the composite algorithms was carried out in two steps. First, the original Sea*UV*/Sea*UVc* set was implemented on the $R_{rs}(\lambda)$ of samples with *in situ* $K_d(490) < 0.32$ m^{-1}. The inshore-water optimized Sea*UV*/Sea*UVc* set was then implemented on the $R_{rs}(\lambda)$ of waters defined as optically complex, that is with *in situ* $K_d(490) > 0.32$ m^{-1}. The $R_{rs}(\lambda)$ data were used as input for the composite Sea*UV*/Sea*UVc* algorithms and the calculated K_d values were then compared with measured K_d values for performance assessment.

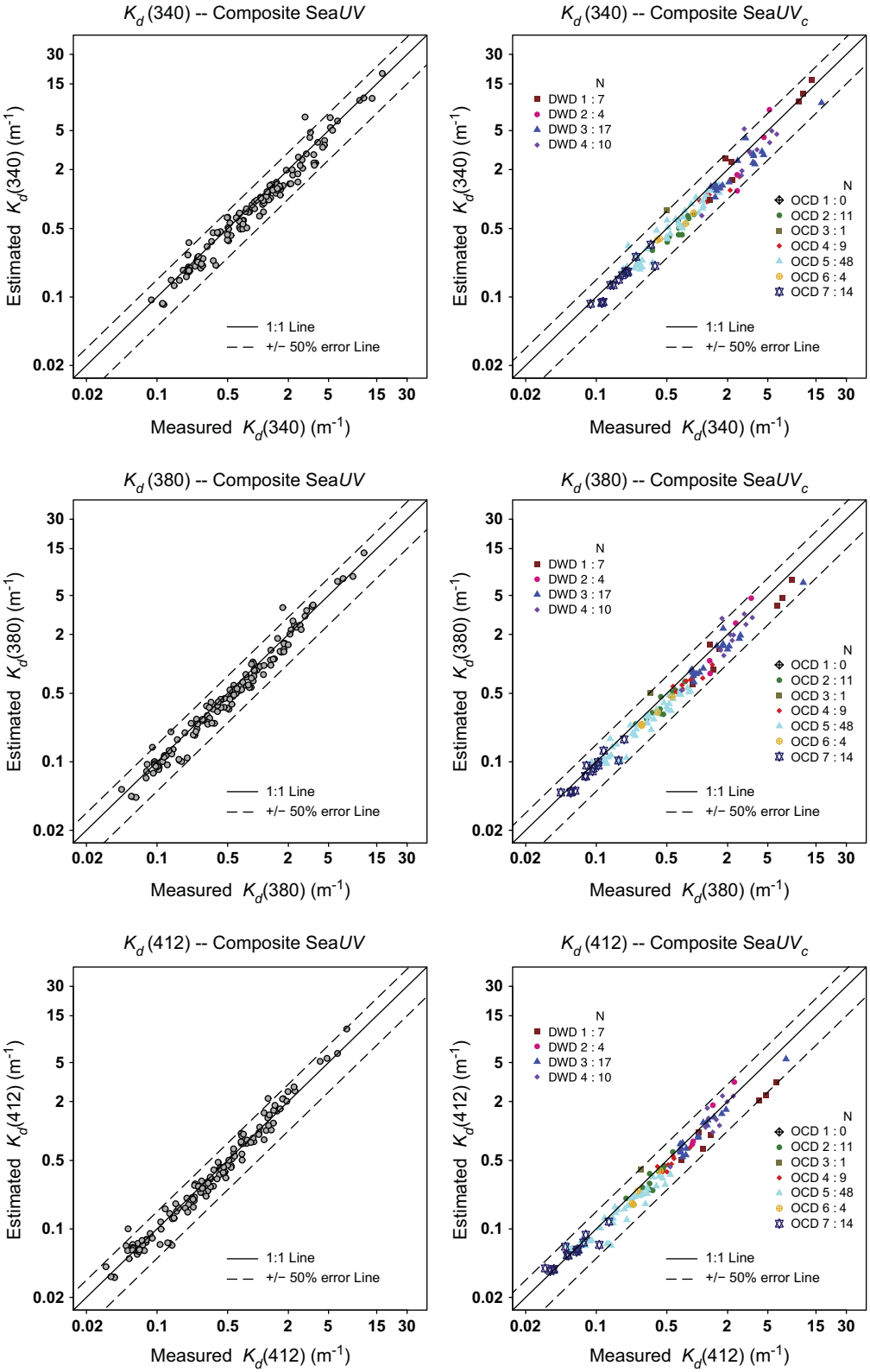

Fig. 8. Comparisons of measured *in situ* K_d with calculated K_d derived from the composite Sea*UV*/Sea*UVc* algorithms at $\lambda = 340$, 380 and 412 nm for the *in situ* validation data set ($N = 125$).

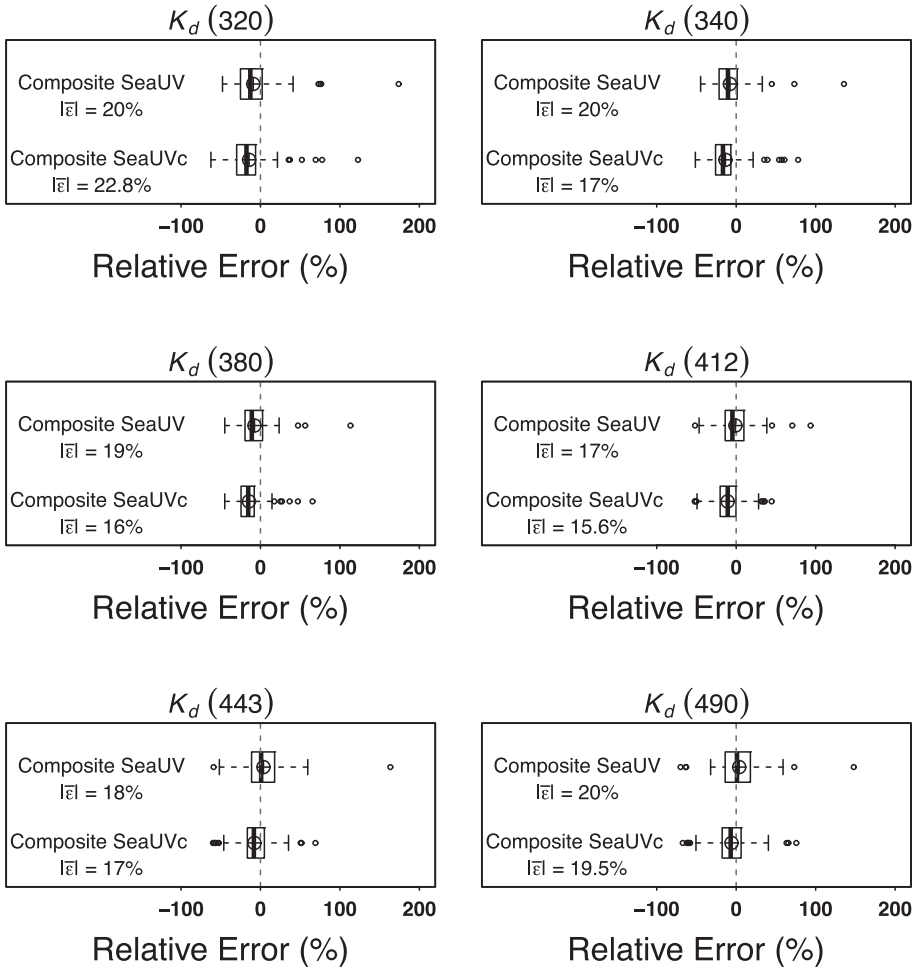

Fig. 9. Box and whisker plots of relative error distribution of K_d derived from the composite Sea*UV*/Sea*UVc* at λ = 320, 340, 380, 412, 443 and 490 nm for the *in situ* validation data set ($N = 125$). Symbols are the same as in Fig. 6.

Fig. 8 shows the results for comparisons between calculated K_d derived from the composite Sea*UV*/Sea*UVc* algorithms and measured *in situ* K_d at λ = 340, 380 and 412 nm for the validation data set. Fig. 9 shows the error analysis for our K_d retrievals associated with the composite Sea*UV*/Sea*UVc* algorithms, indicating good performance at all wavelengths for the validation data set. For $K_d(412)$, the mean relative error derived from the composite Sea*UVc* model is 16% for the validation data set, compared with 16.4% for our complete training data set. The consistent error distribution between the validation and training data set further confirms that the inshore-water optimized Sea*UV*/Sea*UVc* algorithms were well parameterized for higher K_d retrieval in optically complex inshore waters. It is important to note that while the inshore-water optimized Sea*UV*/Sea*UVc* model was developed using AOPs collected along coastal Georgia, these calculations also performed well for K_d retrieval in other inshore waters from diverse locations. The results from the independent *in situ* validation data set demonstrate that inshore-water optimized Sea*UV*/Sea*UVc* may be relatively insensitive to the spatial variation of optical properties. It should also be noted here that the attenuation values for the validation data fall within the range used to parameterize the inshore-water optimized Sea*UV*/Sea*UVc* algorithms (e.g. the western branch of the Mackenzie River and Gulf of Maine, with $K_d(340) \sim 17.0\ m^{-1}$). The good performance for calculations of optically complex water K_d, together with the fact that composite algorithms were parameterized based on a complete training data set that covered an extremely wide range of K_d values, indicate the potential for use of the composite algorithms in K_d retrieval varying from open ocean waters to optically complex inshore waters on a global scale.

3.6. Optimized composite SeaUV algorithms

In light of the empirical nature of the composite Sea*UV*/Sea*UVc* algorithms, the composite algorithms can always be updated using additional data in order to further improve the accuracy of K_d retrievals. Here, the original training and *in situ* validation data sets used by Fichot et al. (2008), and the inshore-water and *in situ* validation data sets compiled for this study were pooled together and used to parameterize a final set of Sea*UV*/Sea*UVc* algorithms. This final set of Sea*UV* algorithms is referred to here as the "optimized composite Sea*UV* algorithms". The parameters associated with this set of algorithms were derived from a data set that covers water types ranging from very oligotrophic open ocean water to optically complex inshore locations ($N = 563$). As shown in Figs. 10 and 11, the optimized composite algorithms performed very well at all wavelengths and performed even better than the algorithms derived from the smaller training data set ($N = 438$). The optimized result obtained by adding the validation data set to the final pool used to derive the composite algorithms also eliminated the biases that occurred in the earlier validation step. Thus, this final optimization of the composite Sea*UV*/Sea*UVc* model parameters is the best product we can provide for the optical community using this approach. A complete scheme of how the optimized composite algorithms should be implemented is provided in Appendix A.

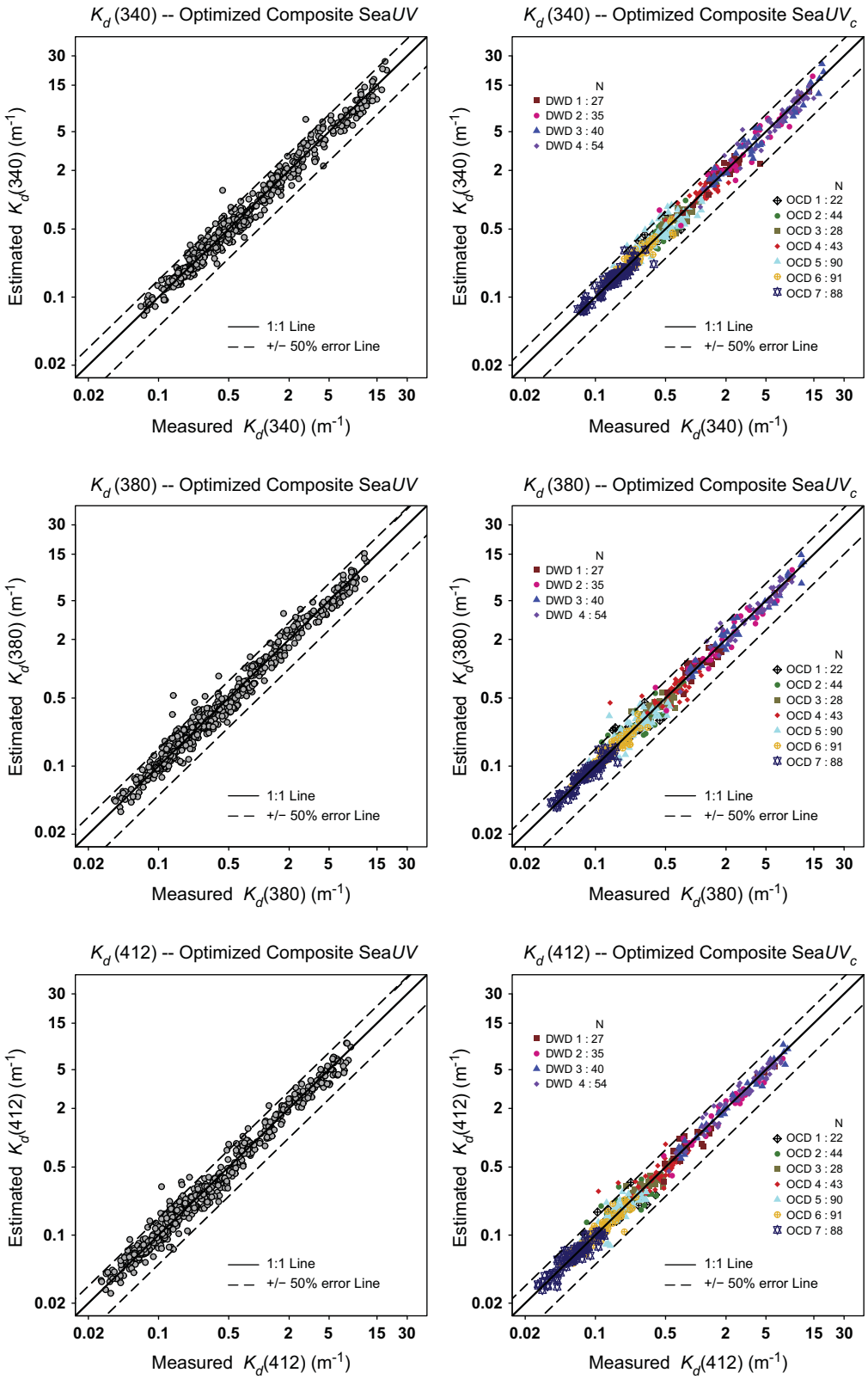

Fig. 10. Comparisons of measured *in situ* K_d with calculated K_d derived from the optimized composite Sea*UV*/Sea*UVc* algorithms at $\lambda = 340$, 380 and 412 nm for the large training data set ($N = 563$).

3.7. Application to SeaWiFS satellite imagery

The optimized composite Sea*UV* algorithm was implemented using SeaWiFS R_{rs} in order to test its applicability with satellite imagery. The monthly climatology of SeaWiFS *Rrs* over the Northern Gulf of Mexico (nGoM) for April 1998–2010 (Level-3, binned 9 × 9 km spatial resolution) was acquired from the NASA ocean color project website (http://oceancolor.gsfc.nasa.gov) and used in this application. The nGoM was chosen because it encompasses oligotrophic waters as well as turbid, high CDOM waters influenced by the Mississippi/Atchafalaya River

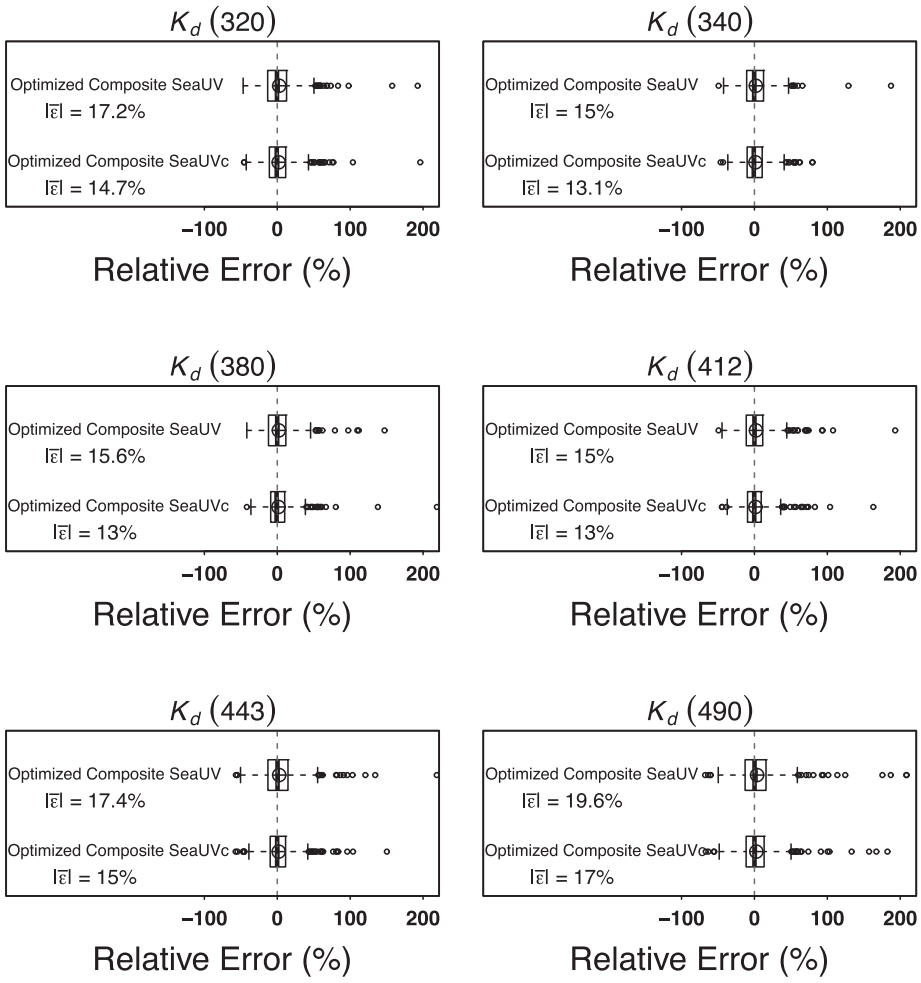

Fig. 11. Box and whisker plots of relative error distribution of K_d derived from the optimized composite Sea*UV*/Sea*UVc* at λ = 320, 340, 380, 412, 443 and 490 nm for the large training data set ($N = 563$). Symbols are the same as in Fig. 6.

plumes (Lohrenz et al., 1999), thus making it a suitable area to demonstrate the overall performance of the optimized composite Sea*UV* algorithms over a wide range of K_d values. Both the original and final optimized composite Sea*UV* algorithms were applied to the SeaWiFS climatological R_{rs} data to derive K_d (noted as $K_d^{original}$ and $K_d^{composite}$ respectively in the following text). For additional comparison, we applied the Jamet et al. (2012) neural network inversion algorithms, also tuned for retrieving K_d (K_d^{NN}) in both open ocean and optically complex waters, to the same SeaWiFS *Rrs*.

Fig. 12 shows the climatology images for comparison. As expected, K_d derived with the original Sea*UV* algorithm (Fig. 12(a) & (d)) displays less variability between the clear offshore Gulf water and waters near the river mouth. However, the images derived using the optimized composite Sea*UV* algorithm (Fig. 12(b) & (e)) show distinct K_d characteristics when applied to different water types, especially in nearshore areas. For $K_d(320)$, the difference in the images derived using original and optimized composite Sea*UV* algorithms can be as large as 100% (Fig. 12(c)). Because K_d^{NN} can only be retrieved at visible wavelengths, we generated images at $K_d(412)$ for $K_d^{composite}$ and K_d^{NN} (Fig. 12(f)) for comparison. $K_d^{NN}(412)$ showed similar patterns overall, but generated slightly higher values than $K_d^{composite}(412)$ for nearshore waters. While $K_d(412)$ is somewhat useful for examining waters with high CDOM content, the distinct advantage of our composite Sea*UV* algorithms is its ability to retrieve K_d in the UV directly from R_{rs}, and in doing so provide essential data for evaluating photochemical production and photobiological reactions in the surface ocean.

4. Summary and conclusions

This study makes two contributions to the ocean optical community by providing improved capacity to retrieve K_d from the most oligotrophic open ocean waters to dynamic inshore systems. First, it reparameterizes the original Sea*UV*/Sea*UVc* algorithms by pooling a new training data set collected in optically complex waters to achieve greatly improved accuracy of $K_d(\lambda)$ retrieval at λ = 320, 340, 380, 412, 443 and 490 nm for turbid coastal waters from ocean color ($R_{rs}(\lambda)$ at SeaWiFS bands, with wavebands centered at λ = 412, 443, 490, 510, 555 and 670 nm). Second, it updates the parameters defined and reported in the original Sea*UV*/Sea*UVc* by using an expanded training data set. The optimization of the original algorithm further enhanced the K_d retrieval accuracy in almost all oceanic and coastal waters. The utilization of such a large training data set that includes an extensive range of K_d values, together with the inherent advantage of the statistical methods employed in developing these algorithms, results in a final Sea*UV*/Sea*UVc* product (namely, the "optimized composite Sea*UV*/Sea*UVc* algorithms") that is suitable for retrieval of K_d over large spatial scales, and in almost any water type.

While good accuracy in retrieving K_d is realized using the new optimized composite Sea*UV* algorithms, readers applying these algorithms to ocean color data should remain aware of several assumptions and issues related to this model. First, as discussed in Fichot et al. (2008), PCA and cluster analysis are purely statistical (empirical) approaches, thus, they neither categorize water types *a priori* nor exclude samples

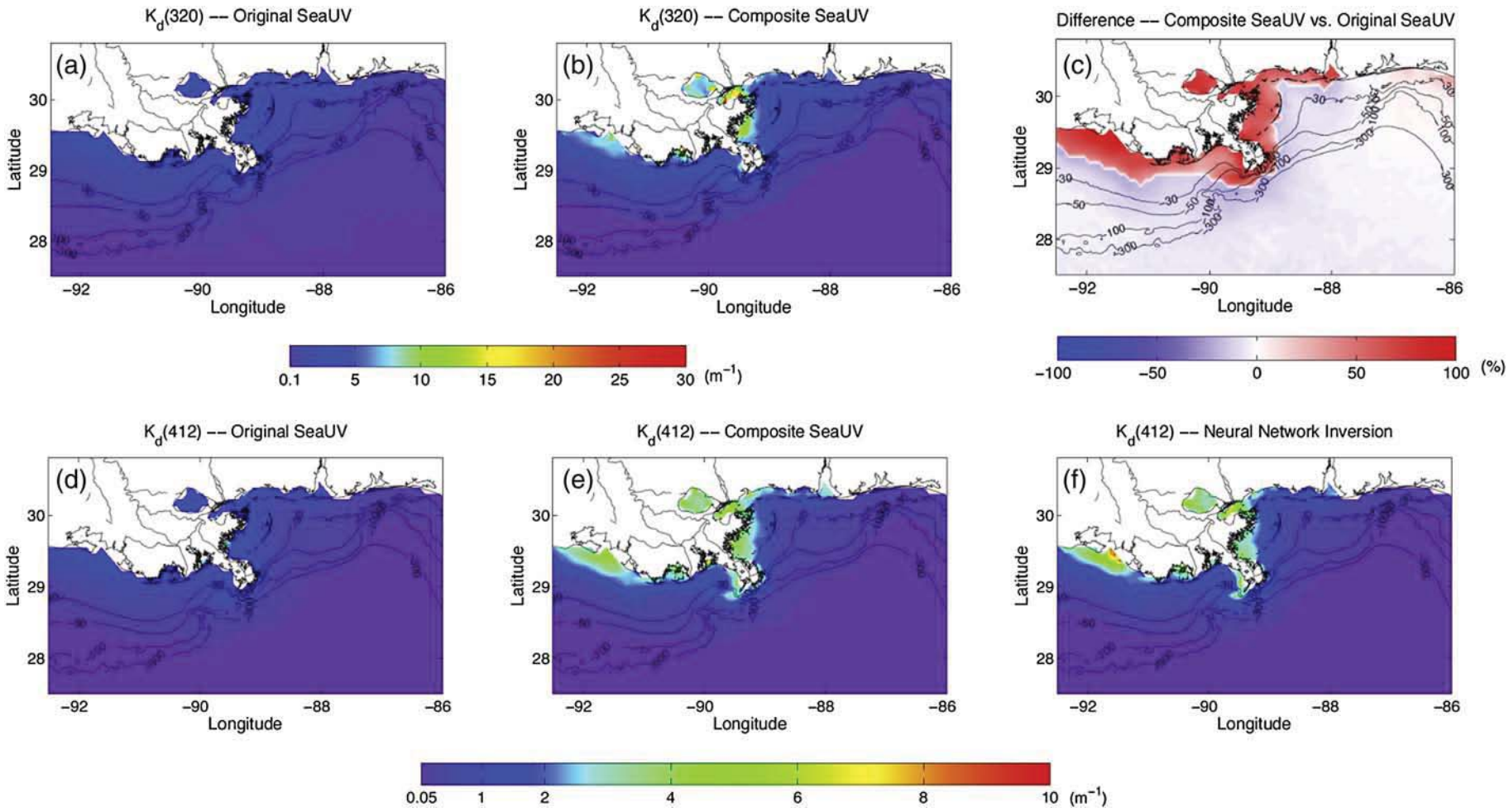

Fig. 12. April climatology (in the period from 1998 to 2010) of $K_d(320)$ and $K_d(412)$ (m^{-1}) derived from SeaWiFS satellite images for the northern Gulf of Mexico using (a) the original Sea*UV* algorithm as published by Fichot et al. (2008) for $K_d(320)$, (b) the optimized composite Sea*UV* algorithm developed in this study for $K_d(320)$, (c) the difference between the optimized composite Sea*UV* and the original Sea*UV* algorithms for $K_d(320)$, the difference was calculated as $\frac{\left(K_d^{compositeSeaUV}-K_d^{originalSeaUV}\right)}{\left(K_d^{compositeSeaUV}+K_d^{originalSeaUV}\right)/2}$, (d) the original Sea*UV* algorithm as published by Fichot et al. (2008) for $K_d(412)$, (e) the optimized composite Sea*UV* algorithm developed in this study for $K_d(412)$ and (f) the neural network inversion method developed by Jamet et al. (2012) for $K_d(412)$. The bathymetry and coastline data were downloaded from the NOAA National Geophysical Data Center (http://www.ngdc.noaa.gov/mgg/bathymetry/relief.html and http://www.ngdc.noaa.gov/mgg/shorelines/shorelines.html).

collected under specific optical situations (i.e. bottom reflectance, turbidity, algal blooms, etc.). Sea*UV*/Sea*UVc* is designed primarily to retrieve K_d in the UV wavelengths based on PCA and cluster analysis. Neither of these statistical approaches requires or, in fact allows underlying assumptions on the spectral data used for the analysis. Interpreting the resulting PC curves or optical domains beyond the design of the model requires speculation that we do not always have auxiliary data to support. The final training data set ($N = 563$) used to derive the algorithm parameters in this paper incorporate an extreme range of marine K_d values, but does not include all water types. For example, including data such as that from the Biogeochemistry and Optics South Pacific Experiment (BIOSOPE) form the clearest oceanic water in the South Pacific subtropical gyre (Morel, Claustre, Antoine, & Gentili, 2007; Morel, Gentili, et al., 2007), may improve model performance for this specific area.

Second, while the optimized PCs defined here best describe the original data when applied together, each individual PC may not necessarily be linearly correlated to any specific inherent optical property (IOP), as pointed out by Toole and Siegel (2001). In the framework of linear algebra, PCA *per se*, only retains the linearity in the training data set, and may not rigorously describe the physical relationship between R_{rs} and IOPs (Morel, 1998; Mueller, 1976). Because the primary purpose of Sea*UV*/Sea*UVc* is to provide the most accurate UV radiation field possible from remotely sensed visible wavelengths, this is not a critical concern. It does, however, remain unknown as to how well the Sea*UV*/Sea*UVc* algorithms predict specific non-linearities between ocean color and IOPs. Third, readers should also be reminded that K_d is an AOP and varies with sun elevation. Most of the data in the training data set were collected with SZA between 0° and 45°, with a few cases occurred with SZA greater than 60°, and any variation was captured implicitly by PCA. Sea*UV*/Sea*UVc* should, however, be used with caution when SZA falls beyond this range.

With the advent of new remote-sensing technologies and the focus on coastal ocean processes, the composite Sea*UV*/Sea*UVc* algorithms will find applicability for the retrieval of K_d in turbid coastal waters using instruments such as the Hyperspectral Imager for the Coastal Ocean (HICO) (Gitelson, Gao, Li, Berdnikov, & Saprygin, 2011; Lucke et al., 2011), the Visible Infrared Imager Radiometer Suite (VIIRS), or the Portable Remote Image Spectrometer (PRISM). Accurate K_d estimates from ocean color can provide better UV data for calculation of photochemical fluxes in coastal waters and address the role of estuarine and coastal waters in photochemical and biogeochemical processes. In addition, spectral UV distribution in the water column can also be modeled using accurate values of K_d by assuming an exponential decrease of K_d values over increasing wavelengths if surface downwelling irradiance is known (Kjeldstad et al., 2003; Markager & Vincent, 2000). These depth profiles are important for quantitative evaluation of UVR inhibition of photosynthesis, bacterial production (Ogbebo & Ochs, 2008) and viral growth (Fuhrman & Noble, 1995) in ecological studies. These algorithms can help to clarify and assess possible effects of UVR in different trophic levels (Yuan, Yin, Harrison, & Zhang, 2011) and in important biogeochemical processes occurring in optically complex waters.

Acknowledgments

This work was funded by grants from the Office of Naval Research (N00140610219), NASA (NNX07AD85G) and Georgia Sea Grant (R/SD-5) awarded to Dr. W. L. Miller. Validation data from the Gulf of Mexico were collected by C. Fichot and S. Lohrenz during the GulfCarbon cruises (2009–2010), funded by the NSF (OCE-0752254), and an NSF award to Drs. R. Benner and W. L. Miller (OCE-0850677). We thank Leanne Powers and Joanna Green, as well as Ike Sellers, Mary Price, and Jason Johnson (UGA Marine Institute) for assistant with sampling aboard the R/V Mud Minnow in coastal Georgia. We thank NASA for providing access to SeaWiFS data. SeaWiFS data were used in accordance with the SeaWiFS data access authorization policy. We also thank Dr. Adrian Burd for valuable suggestions on earlier versions of the draft. Finally, we thank three anonymous reviewers for careful reviews of this manuscript.

Appendix A. Implementation schemes for composite Sea*UV*/Sea*UVc* algorithms

A.1. Required inputs

The remote-sensing reflectance, $R_{rs}(\lambda,0^+)$, measured at $\lambda = 412$, 443, 490, 510, 555 and 670 nm (SeaWiFS wavebands) is required for initial input to the algorithms. Normalized water-leaving radiance $nL_w(\lambda)$ can be converted into $R_{rs}(\lambda,0^+)$ as follows: $R_{rs}(\lambda,0^+) = nL_W(\lambda)/\overline{F_O}(\lambda)$ where the values for the mean extraterrestrial solar flux, $\overline{F_O}(\lambda)$, are provided in Thuillier et al. (2003).

A.2. Retrieving $K_d(490)$ using the NASA $K_d(490)$ algorithm

The measured remote-sensing reflectance $R_{rs}(\lambda,0^+)$ data are first processed through the NASA $K_d(490)$ algorithm (Werdell, 2009) to determine the appropriate set of composite algorithms for use. If the calculated $K_d(490)$ value is lower than 0.32 m^{-1}, the water is classified as "clear" and the first part in the new composite set of Sea*UV* algorithms is used for $K_d(\lambda)$ retrieval. If the calculated $K_d(490)$ is greater than or equal to 0.32 m^{-1}, the water is classified as optically complex inshore water and the inshore-water optimized Sea*UV* (i.e. the second part in the new composite set of Sea*UV* algorithms) is applied for $K_d(\lambda)$ retrieval.

A.3. Retrieving $K_d(\lambda)$ using original SeaUV

For "clear" water, the original Sea*UV*/Sea*UVc* model is implemented on the $R_{rs}(\lambda,0^+)$ values using the same procedure as described in Appendix *C.1.* and *C. 2.* in Fichot et al. (2008). As stated in the text, we have taken advantage of the empirical nature of the Sea*UV* algorithms and updated all parameters used in the original Sea*UV* algorithm with the exception of the cluster centers coordinates, which proved robust, with relocation giving no significant improvement to the statistical fit for the training data. The values of $\overline{R}(\lambda)$ and $\sigma_R(\lambda)$ calculated for standardization from our largest training data set ($N = 563$) are given in Table A.1. The resulting standardized log-linearized remote-sensing reflectances, $X(\lambda)$, can then be used in linear combinations to calculate the scores of the first four principal components. The eigenvectors derived from our large training data set through PCA are used as the correlation coefficients for the multi-linear combinations. The PC scores are updated (Table A.2.) and calculated as in Eq. (1) in Fichot et al. (2008) (e.g. PC score on the first principal component is computed as

$$[PC1]_i = e_{11}X_i(412) + e_{12}X_i(443) + e_{13}X_i(490) + e_{14}X_i(510) + e_{15}X_i(555) + e_{16}X_i(670)),$$

where $e_{11} = -0.3976$, $e_{12} = -0.4237$, $e_{13} = -0.4521$, $e_{14} = -0.4540$, $e_{15} = -0.4159$, $e_{16} = -0.2809$. Scores on PC2, PC3 and PC4 are calculated similarly and are then used as the independent variables in the multilinear regressions to predict K_d. The correlation coefficients (parameters $\alpha, \beta, \gamma, \delta, \varepsilon$) have been updated and are provided in Table A.3. For the clear water Sea*UVc* model, the cluster centers in the updated Sea*UVc* are the same as published in Fichot et al. (2008). The observations are assigned to their optical domains using the first two PC scores and log-linearized $K_d(\lambda)$ is calculated by using Eq. (4) in Fichot et al. (2008) with the updated parameters corresponding to the identified optical domains provided in here Tables A.4, A.5 and A.6.

A.4. Retrieving $K_d(\lambda)$ using inshore-water optimized SeaUV/SeaUVc

If the calculated $K_d(490)$ is greater than or equal to 0.32 m^{-1} and the water is classified as optically complex, inshore water, the new inshore-water optimized Sea*UV*/Sea*UVc* model provides a much more accurate retrieval of $K_d(\lambda)$. The inshore-water optimized Sea*UV* model is then used with similar logic to that used for implementation of the original Sea*UV* (as described in Fichot et al. (2008)). The parameters for standardization, calculation of PC scores and multi-linear coefficients are provided in Tables A.7, A.8 and A.9. For the inshore-water optimized Sea*UVc* algorithms, four dark water domains (DWDs) are defined for retrieving $K_d(\lambda)$. The coordinates of the four cluster centers in inshore-water optimized *SeaUVc* are provided in Table A.10. Each observation is assigned to the appropriate DWD by using the first two PC scores, allowing the log-linearized $K_d(\lambda)$ value to be calculated using Eq. (4) in Fichot et al. (2008) using the updated parameters for use in corresponding to the dark water domain provided here in Tables A.11, A.12 and A.13.

Table A.1
Updated mean and standard deviations to center and standardize $\ln(R_{rs}(\lambda,0^+))$ for the original Sea*UV*/Sea*UVc* algorithms.

	λ = 412	λ = 443	λ = 490	λ = 510	λ = 555	λ = 670
$\bar{R}(\lambda)$	−5.3340	−5.2589	−5.0970	−5.2474	−5.5939	−7.9649
$\sigma_R(\lambda)$	0.8637	0.7808	0.7268	0.7483	0.8208	0.8836

Table A.2
Updated first four eigenvectors for use in calculating the PC scores for the "original" Sea*UV*/Sea*UVc* algorithms.

	λ = 412	λ = 443	λ = 490	λ = 510	λ = 555	λ = 670
e_1	−0.3976	−0.4237	−0.4521	−0.4540	−0.4159	−0.2809
e_2	0.4481	0.3497	0.1303	−0.0670	−0.3652	−0.7226
e_3	0.3990	0.2370	−0.1326	−0.3724	−0.4920	0.6215
e_4	0.5829	−0.2240	−0.5733	−0.1354	0.5045	−0.0928

Table A.3
Updated parameters for retrieval of $\ln(K_d(\lambda))$ from the PC scores in the original Sea*UV* algorithms.

	α	β	γ	δ	ε
$\ln(K_d(320))$	−0.7327	0.0980	−0.5928	−0.5230	−1.1130
$\ln(K_d(340))$	−1.0625	0.0855	−0.6301	−0.4996	−0.8653
$\ln(K_d(380))$	−1.6508	0.0485	−0.6565	−0.4154	−0.4186
$\ln(K_d(412))$	−1.9638	0.0240	−0.6550	−0.3240	0.1644
$\ln(K_d(443))$	−2.1846	0.0088	−0.6256	−0.2368	0.6171
$\ln(K_d(490))$	−2.4894	−0.0025	−0.5574	−0.0733	0.6902

Table A.4
Updated parameters for retrieval of $\ln[K_d(\lambda)]$ (λ = 320 and 340 nm) from the PC scores in the original Sea*UVc* algorithms.

	α	β	γ	δ	ε
$\ln[K_d(320)]$					
OCD1	−0.7880	0.0555	−0.6148	−0.3852	−0.7067
OCD2	−0.8138	0.1098	−0.6411	−0.6162	−0.9544
OCD3	−0.6073	0.1372	−0.5505	−0.1169	−1.7478
OCD4	−0.7821	0.1357	−0.5775	−0.4700	−0.5023
OCD5	−0.4816	−0.0044	−0.5721	−0.6300	−1.1761
OCD6	−0.8359	0.1386	−0.4460	−0.6736	−0.9057
OCD7	−0.7764	0.1411	−0.5378	−0.6900	−0.8205
$\ln[K_d(340)]$					
OCD1	−1.0733	0.0588	−0.6328	−0.3243	−0.6286
OCD2	−1.1055	0.0981	−0.6514	−0.5232	−0.7947
OCD3	−0.8734	0.1260	−0.5453	−0.1725	−1.7031
OCD4	−1.1280	0.1202	−0.6284	−0.5058	−0.4116
OCD5	−0.9525	0.0376	−0.6103	−0.5717	−1.0074
OCD6	−1.1507	0.1015	−0.5148	−0.5969	−0.6982
OCD7	−1.0968	0.1140	−0.5800	−0.7075	−0.6110

Table A.5
Updated parameters for retrieval of $\ln[K_d(\lambda)]$ (λ = 380 and 412 nm) from the PC scores in the original Sea*UVc* algorithms.

	α	β	γ	δ	ε
$\ln[K_d(380)]$					
OCD1	−1.6649	0.0356	−0.6626	−0.1942	−0.2820
OCD2	−1.6453	0.0542	−0.6710	−0.3232	−0.5304
OCD3	−1.2807	0.1287	−0.5558	−0.2712	−1.9238
OCD4	−1.8815	0.0860	−0.7529	−0.4659	0.4369
OCD5	−1.5699	0.0055	−0.5469	−0.6102	−0.7134
OCD6	−1.7408	0.0601	−0.5786	−0.6292	−0.2607
OCD7	−1.7133	0.0770	−0.5789	−0.6661	−0.2665
$\ln[K_d(412)]$					
OCD1	−2.066	−0.0117	−0.5788	−0.0081	0.1561
OCD2	−1.9402	0.0273	−0.6691	−0.1097	−0.0423
OCD3	−1.5982	0.1176	−0.5712	−0.0780	−1.3923
OCD4	−2.1512	0.0492	−0.7311	−0.2785	0.4277
OCD5	−1.9057	−0.0093	−0.5560	−0.6052	−0.1428
OCD6	−2.0421	0.0255	−0.6314	−0.5377	0.4598
OCD7	−2.0247	0.0667	−0.5683	−0.6719	0.0959

Table A.6
Updated parameters for retrieval of $\ln[K_d(\lambda)]$ (λ = 443 and 490 nm) from the PC scores in the original Sea*UVc* algorithms.

	α	β	γ	δ	ε
$\ln[K_d(443)]$					
OCD1	−2.4117	−0.0551	−0.5317	0.0673	0.6669
OCD2	−2.1752	0.0009	−0.6672	0.0970	0.2309
OCD3	−1.7932	0.1273	−0.5862	0.0473	−1.0485
OCD4	−2.4883	0.1158	−0.6174	−0.3085	0.9051
OCD5	−2.1744	−0.0030	−0.5205	−0.5934	0.4998
OCD6	−2.2708	−0.0002	−0.6345	−0.4557	1.0245
OCD7	−2.2943	0.0654	−0.4923	−0.6039	0.4254
$\ln[K_d(490)]$					
OCD1	−3.0337	−0.1438	−0.5119	0.0357	1.7743
OCD2	−2.5423	−0.0575	−0.6011	0.3010	0.3775
OCD3	−2.1348	0.1232	−0.5911	0.2175	−1.0509
OCD4	−2.6192	0.0104	−0.5910	−0.3303	0.8374
OCD5	−2.5163	0.0150	−0.3711	−0.4385	0.8056
OCD6	−2.5759	−0.0115	−0.6348	−0.2714	1.0642
OCD7	−2.6486	0.0952	−0.3854	−0.4047	0.5484

Table A.7
Updated mean and standard deviations to center and standardize $\ln(R_{rs}(\lambda,0^+))$ for the inshore-water optimized Sea*UV*/Sea*UVc* algorithms.

	λ = 412	λ = 443	λ = 490	λ = 510	λ = 555	λ = 670
$\bar{R}(\lambda)$	−6.8156	−6.3098	−5.6367	−5.4596	−5.0692	−5.9379
$\sigma_R(\lambda)$	1.0703	0.9956	0.8839	0.8599	0.7490	0.7485

Table A.8
Updated first four eigenvectors for use in calculating the PC scores for the inshore-water optimized Sea*UV*/Sea*UVc* algorithms.

	λ = 412	λ = 443	λ = 490	λ = 510	λ = 555	λ = 670
e_1	−0.4019	−0.4224	−0.4295	−0.4297	−0.4240	−0.3333
e_2	−0.4536	−0.2541	−0.0825	−0.0403	0.1504	0.8358
e_3	0.5303	0.2160	−0.1431	−0.3003	−0.6103	0.4347
e_4	−0.4941	0.2907	0.4526	0.3252	−0.6005	−0.0113

Table A.9
Updated parameters for retrieval of $\ln(K_d(\lambda))$ from the PC scores in the inshore-water optimized Sea*UV* algorithm.

	α	β	γ	δ	ε
$\ln(K_d(320))$	1.7574	0.1253	1.0342	−0.3073	0.8648
$\ln(K_d(340))$	1.4696	0.1181	0.9701	−0.1030	0.6973
$\ln(K_d(380))$	0.9983	0.1117	0.9816	0.1098	0.5601
$\ln(K_d(412))$	0.6930	0.1200	0.9512	0.3410	0.0220
$\ln(K_d(443))$	0.4314	0.1130	0.9268	0.4504	−0.2891
$\ln(K_d(490))$	0.0530	0.0927	0.9158	0.5754	−0.3118

Table A.10
Coordinates of the cluster centers corresponding to the four dark water domains defined in this study for the inshore-water optimized Sea*UVc* algorithms.

n	X_n (PC1)	Y_n (PC2)
DWD1	−4.4836	−0.2043
DWD2	0.8671	−0.3379
DWD3	2.2617	−0.0836
DWD4	−0.0862	0.6324

Table A.11
Updated parameters for retrieval of $\ln[K_d(\lambda)]$ ($\lambda = 320$ and 340 nm) from the PC scores in the inshore-water optimized Sea*UVc* algorithms.

	α	β	γ	δ	ε
$\ln[K_d(320)]$					
DWD1	1.8181	0.1394	0.9296	0.0974	0.1340
DWD2	1.4925	0.4003	1.1138	−0.5654	0.9708
DWD3	1.8445	0.0797	0.8835	−0.9424	0.9792
DWD4	1.8433	0.2955	0.9879	0.0173	0.4808
$\ln[K_d(340)]$					
DWD1	1.4029	0.0950	0.9244	0.2621	−0.1177
DWD2	1.2840	0.3588	1.0551	−0.2270	0.9539
DWD3	1.4194	0.1288	0.8501	−0.6873	0.7522
DWD4	1.5157	0.2423	0.9216	0.1778	0.2762

Table A.12
Updated parameters for retrieval of $\ln[K_d(\lambda)]$ ($\lambda = 380$ and 412 nm) from the PC scores in the inshore-water optimized Sea*UVc* algorithms.

	α	β	γ	δ	ε
$\ln[K_d(380)]$					
DWD1	0.8770	0.0888	0.8222	0.5918	−0.7150
DWD2	0.9102	0.2414	1.0345	−0.0173	0.7401
DWD3	0.8756	0.1416	0.8838	−0.5368	0.6536
DWD4	1.0861	0.2472	0.8983	0.5389	0.3796
$\ln[K_d(412)]$					
DWD1	0.8069	0.1642	0.7620	0.5546	−1.2081
DWD2	0.6699	0.1845	0.9643	0.2231	0.2031
DWD3	0.6022	0.1261	0.8923	−0.1241	0.1357
DWD4	0.8078	0.2412	0.8606	0.8385	−0.0013

Table A.13
Updated parameters for retrieval of $\ln[K_d(\lambda)]$ ($\lambda = 443$ and 490 nm) from the PC scores in the inshore-water optimized Sea*UVc* algorithms.

	α	β	γ	δ	ε
$\ln[K_d(443)]$					
DWD1	0.5266	0.1574	0.6767	0.6478	−1.5230
DWD2	0.4115	0.1525	0.9055	0.3685	−0.1893
DWD3	0.3490	0.1162	0.8966	0.0601	−0.1541
DWD4	0.5585	0.2460	0.8400	0.9705	−0.1524
$\ln[K_d(490)]$					
DWD1	0.0891	0.1175	0.6923	0.5053	−1.6898
DWD2	0.0144	0.1224	0.8882	0.4612	−0.2901
DWD3	−0.0369	0.1051	0.8915	0.1950	−0.1502
DWD4	0.1827	0.2437	0.8325	1.1980	−0.1505

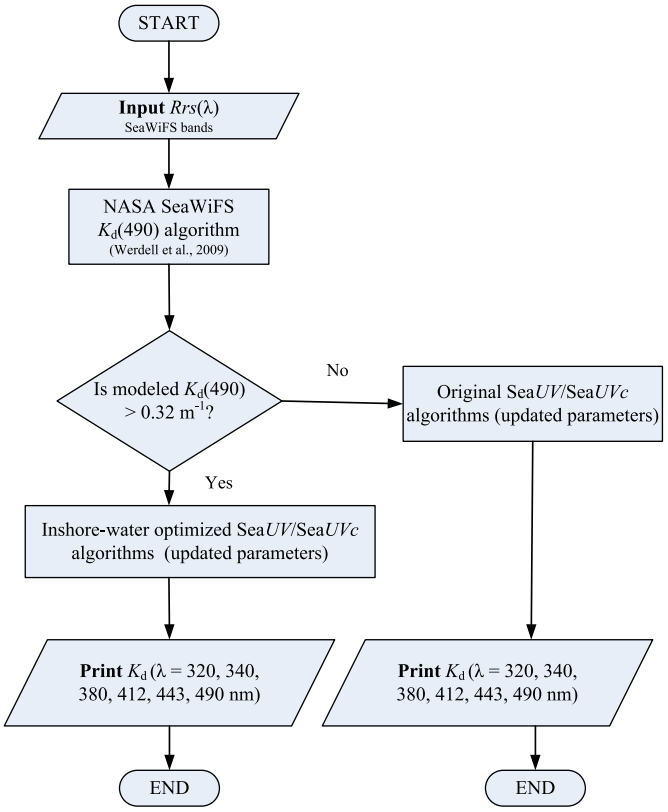

Fig. A1. Flow chart diagram for implementation of optimized composite Sea*UV*/Sea*UVc* algorithms.

Appendix B. Supplementary data

Supplementary data to this article can be found online at http://dx.doi.org/10.1016/j.rse.2014.01.003.

References

Austin, R. W. (1974). The remote sensing of spectral radiance from below the ocean surface. In N. G. Jerlov (Ed.), *Optical aspects of oceanography* (pp. 317–344). London: Academic Press.
Austin, R. W., & Petzold, T. J. (1981). The determination of the diffuse attenuation coefficient of sea water using the coastal zone color scanner. In J. F. R. Grower (Ed.), *Oceanography from space* (pp. 239–256). New York: Plenum Press.
Booth, C. R., & Morrow, J. H. (1997). The penetration of UV into natural waters. *Photochemistry and Photobiology*, *65*(2), 254–257.
Craft, C. (2007). Freshwater input structures soil properties, vertical accretion, and nutrient accumulation of Georgia and US tidal marshes. *Limnology and Oceanography*, *52*(3), 1220–1230.
Fichot, C. G., & Miller, W. L. (2010). An approach to quantify depth-resolved marine photochemical fluxes using remote sensing: Application to carbon monoxide (CO) photoproduction. *Remote Sensing of Environment*, *114*(7), 1363–1377.
Fichot, C. G., Sathyendranath, S., & Miller, W. L. (2008). SeaUV and SeaUVc: Algorithms for the retrieval of UV/visible diffuse attenuation coefficients from ocean color. *Remote Sensing of Environment*, *112*(4), 1584–1602.
Fuhrman, J. A., & Noble, R. T. (1995). Viruses and protists cause similar bacterial mortality in coastal seawater. *Limnology and Oceanography*, *40*(7), 1236–1242.
Gitelson, A. A., Gao, B. C., Li, R. R., Berdnikov, S., & Saprygin, V. (2011). Estimation of chlorophyll-a concentration in productive turbid waters using a hyperspectral imager for the coastal ocean—The Azov Sea case study. *Environmental Research Letters*, *6*(2), 024023.
Gordon, H. R. (1989). Can the Lambert–Beer law be applied to the diffuse attenuation coefficient of ocean water? *Limnology and Oceanography*, *34*(8), 1389–1409.
Jamet, C., Loisel, H., & Dessailly, D. (2012). Retrieval of the spectral diffuse attenuation coefficient $K_d(\lambda)$ in open and coastal ocean waters using a neural network inversion. *Journal of Geophysical Research*, *117*, C10023, http://dx.doi.org/10.1029/2012JC008076.
Johannessen, S.C., Miller, W. L., & Cullen, J. J. (2003). Calculation of UV attenuation and colored dissolved organic matter absorption spectra from measurements of ocean color.

Journal of Geophysical Research, *108*(C9), 3301, http://dx.doi.org/10.1029/2000JC000514.

Kirk, J. T. O. (1994). *Light and photosynthesis in aquatic ecosystems* (2nd ed.). New York, NY, USA: Cambridge University Press.

Kjeldstad, B., Frette, Ø., Erga, S. R., Browman, H. I., Kuhn, P., Davis, R., et al. (2003). UV (280 to 400 nm) optical properties in a Norwegian fjord system and an intercomparison of underwater radiometers. *Marine Ecology Progress Series*, *256*, 1–11.

Kuhn, P., Browman, H., McArthur, B., & St-Pierre, J. F. (1999). Penetration of ultraviolet radiation in the waters of the estuary and Gulf of St. Lawrence. *Limnology and Oceanography*, *44*(3), 710–716.

Laurion, I., Vincent, W. F., & Lean, D. R. (1997). Underwater ultraviolet radiation: Development of spectral models for northern high latitude lakes. *Photochemistry and Photobiology*, *65*(1), 107–114.

Lee, Z., Du, K., Arnone, R., Liew, S., & Penta, B. (2005). Penetration of solar radiation in the upper ocean: A numerical model for oceanic and coastal waters. *Journal of Geophysical Research*, *110*, C09019, http://dx.doi.org/10.1029/2004JC002780.

Lohrenz, S. E., Fahnenstiel, G. L., Redalje, D.G., Lang, G. A., Dagg, M. J., Whitledge, T. E., et al. (1999). Nutrients, irradiance, and mixing as factors regulating primary production in coastal waters impacted by the Mississippi River plume. *Continental Shelf Research*, *19*(9), 1113–1141.

Lucke, R. L., Corson, M., McGlothlin, N. R., Butcher, S. D., Wood, D. L., Korwan, D. R., et al. (2011). Hyperspectral imager for the coastal ocean: Instrument description and first images. *Applied Optics*, *50*(11), 1501–1516.

Markager, S., & Vincent, W. F. (2000). Spectral light attenuation and the absorption of UV and blue light in natural waters. *Limnology and Oceanography*, *45*(3), 642–650.

Moore, T. S., Campbell, J. W., & Dowell, M.D. (2009). A class-based approach to characterizing and mapping the uncertainty of the MODIS ocean chlorophyll product. *Remote Sensing of Environment*, *113*(11), 2424–2430.

Moore, T. S., Campbell, J. W., & Feng, H. (2001). A fuzzy logic classification scheme for selecting and blending satellite ocean color algorithms. *IEEE Transactions on Geoscience and Remote Sensing*, *39*(8), 1764–1776.

Mopper, K., & Kieber, D. J. (2000). Marine photochemistry and its impact on carbon cycling. In S. de Mora, S. Demers, & M. Vernet (Eds.), *The effects of UV radiation in the marine environment. The effects of UV radiation in the marine environment*. (pp. 101–129). Cambridge, UK: Cambridge University Press.

Morel, A. (1998). *Minimum requirements for an operational ocean-colour sensor for the open ocean. IOCCG Report, Vol. 1*, . Dartmouth, Nova Scotia: IOCCG Project Office (46 pp.).

Morel, A., Claustre, H., Antoine, D., & Gentili, B. (2007). Natural variability of bio-optical properties in case 1 waters: Attenuation and reflectance within the visible and near-UV spectral domains, as observed in South Pacific and Mediterranean waters. *Biogeosciences Discussions*, *4*(4), 2147–2178.

Morel, A., Gentili, B., Claustre, H., Babin, M., Bricaud, A., Ras, J., et al. (2007). Optical properties of the "clearest" natural waters. *Limnology and Oceanography*, *52*(1), 217–229.

Mueller, J. L. (1976). Ocean color spectra measured off the Oregon coast: Characteristic vectors. *Applied Optics*, *15*(2), 394–402.

Mueller, J. L. (2000). SeaWiFS algorithm for the diffuse attenuation coefficient, K(490), using water-leaving radiances at 490 and 555 nm. In S. B. Hooker, & E. R. Firestone (Eds.), *SeaWiFS postlaunch calibration and validation analysis: Part 3. NASA Tech. Memo. 2000-206892, Vol. 11*. (pp. 24–27). Greenbelt, Maryland: NASA Goddard Space Flight Center.

Ogbebo, F. E., & Ochs, C. (2008). Bacterioplankton and phytoplankton production rates compared at different levels of solar ultraviolet radiation and limiting nutrient ratios. *Journal of Plankton Research*, *30*(11), 1271–1284.

Richardson, L. L., & LeDrew, E. F. (Eds.). (2006). *Remote sensing of aquatic coastal ecosystem processes: Science and management applications. Remote sensing and digital image processing, Vol. 9*. (pp. 57). Dordrecht: Springer.

Sinha, R. P., & Häder, D. P. (2002). UV-induced DNA damage and repair: A review. *Photochemical & Photobiological Sciences*, *1*(4), 225–236.

Tedetti, M., & Sempéré, R. (2006). Penetration of ultraviolet radiation in the marine environment. A review. *Photochemistry and Photobiology*, *82*(2), 389–397.

Tedetti, M., Sempéré, R., Vasilkov, A., Charrière, B., Nérini, D., Miller, W. L., et al. (2007). High penetration of ultraviolet radiation in the south east Pacific waters. *Geophysical Research Letters*, *34*, L12610, http://dx.doi.org/10.1029/2007GL029823.

Thuillier, G., Hersé, M., Foujols, T., Peetermans, W., Gillotay, D., Simon, P. C., et al. (2003). The solar spectral irradiance from 200 to 2400 nm as measured by the SOLSPEC spectrometer from the ATLAS and EURECA missions. *Solar Physics*, *214*(1), 1–22.

Toole, D. A., & Siegel, D. A. (2001). Modes and mechanisms of ocean color variability in the Santa Barbara Channel. *Journal of Geophysical Research*, *106*, 26,985–27,000.

Wang, M., Son, S., & Harding, L. W. (2009). Retrieval of diffuse attenuation coefficient in the Chesapeake Bay and turbid ocean regions for satellite ocean color applications. *Journal of Geophysical Research*, *114*, C10011, http://dx.doi.org/10.1029/2009JC005286.

Werdell, P. J. (2009). Diffuse attenuation coefficient (K_d) for downwelling irradiance at 490-nm. http://oceancolor.gsfc.nasa.gov/REPROCESSING/R2009/kdv4/

Whitehead, R. F., de Mora, S. J., & Demers, S. (2000). Enhanced UV radiation—A new problem for the marine environment. In S. de Mora, S. Demers, & M. Vernet (Eds.), *The effects of UV radiation in the marine environment* (pp. 1–34). Cambridge, UK: Cambridge University Press.

Witte, W. G., Whitlock, C. H., Harriss, R. C., Usry, J. W., Poole, L. R., Houghton, W. M., et al. (1982). Influence of dissolved organic materials on turbid water optical properties and remote-sensing reflectance. *Journal of Geophysical Research*, *87*(C1), 441–446.

Yuan, X., Yin, K., Harrison, P. J., & Zhang, J. (2011). Phytoplankton are more tolerant to UV than bacteria and viruses in the northern South China Sea. *Aquatic Microbial Ecology*, *65*(2), 117–128.